Monthly Notices
of the
ROYAL ASTRONOMICAL SOCIETY

MNRAS **528,** 5511–5527 (2024)
Advance Access publication 2024 January 13

https://doi.org/10.1093/mnras/stae137

Modelling stellar variability in archival HARPS data: I - Rotation and activity properties with multidimensional Gaussian processes

Haochuan Yu,[1★] Suzanne Aigrain,[1] Baptiste Klein,[1] Oscar Barragán,[1] Annelies Mortier,[2] Niamh K. O'Sullivan[1] and Michael Cretignier[1]

[1]*Sub-department of Astrophysics, Department of Physics, University of Oxford, Oxford, OX1 3RH, UK*
[2]*School of Physics & Astronomy, University of Birmingham, Edgbaston, Birmingham B15 2TT, UK*

Accepted 2024 January 5. Received 2023 December 21; in original form 2023 October 11

ABSTRACT

Although instruments for measuring the radial velocities (RVs) of stars now routinely reach sub-metre per second accuracy, the detection of low-mass planets is still very challenging. The rotational modulation and evolution of spots and/or faculae can induce variations in the RVs at the level of a few $\mathrm{m\,s^{-1}}$ in Sun-like stars. To overcome this, a multidimensional Gaussian Process framework has been developed to model the stellar activity signal using spectroscopic activity indicators together with the RVs. A recently published computationally efficient implementation of this framework, `S + LEAF 2`, enables the rapid analysis of large samples of targets with sizeable data sets. In this work, we apply this framework to HARPS observations of 268 well-observed targets with precisely determined stellar parameters. Our long-term goal is to quantify the effectiveness of this framework to model and mitigate activity signals for stars of different spectral types and activity levels. In this first paper in the series, we initially focus on the activity indicators (S-index and Bisector Inverse Slope), and use them to (a) measure rotation periods for 49 slow rotators in our sample, (b) explore the impact of these results on the spin-down of middle-aged late F, G, and K stars, and (c) explore indirectly how the spot to facular ratio varies across our sample. Our results should provide valuable clues for planning future RV planet surveys such as the Terra Hunting Experiment or the PLATO ground-based follow-up observations programme, and help fine-tune current stellar structure and evolution models.

Key words: exoplanets – planets and satellites: detection – stars: low-mass – stars: rotation – stars: magnetic fields – techniques: radial velocities.

1 INTRODUCTION

Since the groundbreaking detection of the first exoplanet orbiting a sun-like star, 51 Peg b (Mayor & Queloz 1995), using the radial velocity (RV) method, numerous techniques have been developed and campaigns initiated to discover exoplanets with the ultimate goal of finding another habitable world. The RV method continues to be one of the most promising techniques for detecting Earth-like planets, thanks to the development of optical ultra-stable high-resolution échelle spectrographs such as High Accuracy Radial Velocity Planet Searcher (HARPS; Mayor et al. 2003), HARPS-N (Cosentino et al. 2012), ESPRESSO (Pepe et al. 2021), EXPRES (Jurgenson et al. 2016), NEID (Schwab et al. 2018), and the upcoming KPF (Gibson et al. 2016) and HARPS-3 (Thompson et al. 2016). These new instruments can achieve extreme precision down to $0.3\,\mathrm{ms^{-1}}$ (e.g. Suárez Mascareño et al. 2020; Faria et al. 2022) and even beyond.

However, despite the sub-metre-per-second accuracy achieved by RV instruments, the detection of Earth analogues remains a significant challenge, primarily attributed to stellar activity. For example, in our own Solar system, the amplitude of Earth's RV signal is a mere $0.1\,\mathrm{m\,s^{-1}}$, yet RV fluctuations caused by solar activity can exceed several $\mathrm{m\,s^{-1}}$ (e.g. Meunier, Desort & Lagrange 2010; Haywood et al. 2022). As a result, signals from small, moderately distant planets, similar to Earth, could easily be obscured by the activity of their host star. Accurate modelling of these activity signals is crucial for the successful detection of such planets.

Variations in the RV time-series can arise from a variety of stellar activity processes, often manifesting across different time-scales. Predominantly, these fluctuations are the consequence of the magnetic field of the star interplay with the convection. In the following, we discuss several mechanisms believed to be most crucial in inducing variations in the RVs.

On short time-scales, the surface of an FGKM star consists of cells where local convection occurs, a phenomenon known as granulation. In each cell, material heated up rises to the surface, causing a blueshift in the lines, while cooler material sinks, causing a redshift. Since the hotter material is generally brighter than the cooler material, averaging the line profiles over the stellar surface produces an asymmetric line profile, resulting in a net blueshift when measuring the line centres. As these cells, or granules, evolve stochastically on the stellar surface, this effect can induce RV variations at the $\mathrm{m\,s^{-1}}$ level, with time-scales ranging from a few minutes to several hours (e.g. Dumusque et al. 2011a; Cegla et al. 2013, 2018, 2019; Meunier

---

[★] E-mail: haochuan.yu@physics.ox.ac.uk et al. 2015; Meunier & Lagrange 2019). On even shorter time-scales, surface granulation and magnetic events can excite oscillations of the star at characteristic frequencies (acoustic modes), known as pressure-mode (p-mode) oscillations (e.g. Kjeldsen & Bedding 1995; Arentoft et al. 2008). For sun-like stars, p-mode oscillations can induce RV variations with a period of several minutes and an amplitude of around 0.1–1 m s^{-1} (Strassmeier, Ilyin & Steffen 2018; Cegla 2019). Given that the time-scales of these effects are normally short compared to the orbital period of the planet of interest, such effects can be filtered out by either extending the exposure time (e.g. Chaplin et al. 2019), or binning the data to a lower time resolution.

On moderate time-scales, effects caused by active regions on the stellar surface become significant. These regions are shaped by magnetic fields, which can interfere with the convection on the stellar surface in two ways. First, when the magnetic field suppresses the local heat transport, it results in dark regions known as spots. Secondly, if the magnetic field is not strong enough to entirely suppress the heat transport, it alters local opacity which produces brighter regions, often referred to as faculae or plages. These active regions can induce RV variations through two primary mechanisms: the photometric effect, marked by a localized flux alteration, and the inhibition of the convective blueshift effect, characterized by a reduced blueshift on the local line profile. Therefore, disc-integrated line profiles exhibit distortion due to these localized changes, manifesting as shifts in the RV. As these active regions rotate with the surface of the star, the induced RV signal is modulated by such rotation, resulting in a signal with quasi-periodic (QP) variations. Meunier et al. (2010) found that, for the sun, the amplitude of such variation in the RV is around 0.4–1.4 m s^{-1} and is dominated by the convective blueshift effect. The challenge lies in the fact that the rotation periods of sun-like stars can be of the same order of magnitudes as the orbital period of exoplanets. This similarity led to a few early claims being subsequently refuted (e.g. Rajpaul, Aigrain & Roberts 2016).

Several techniques have been developed to mitigate such activity signals. One straightforward approach is to compare the Lomb–Scargle periodograms of RV and spectroscopic activity indicators to visually distinguish between stellar and planetary periods. This method is only effective when the data is relatively regular-sampled and the stellar signal remains less evolved. An alternative approach is to employ Stacked Bayesian General Lomb–Scargle periodograms (Mortier & Collier Cameron 2017), which provides a way to assess the stability of signals over time. Stellar signals can be identified as they are unstable and incoherent, in contrast to planetary signals which are consistent and stable. A more advanced approach is to use a multidimensional Gaussian Process framework, which models the RV together with the activity indicators (e.g. Aigrain, Pont & Zucker 2012; Rajpaul et al. 2015; Barragán et al. 2022). We will delve deeper into this approach in Section 3. Besides, there are techniques that conduct activity mitigation at earlier stages. For instance, some start from cross-correlation function (CCF) (e.g. Donati et al. 2014; Collier Cameron et al. 2021; John, Collier Cameron & Wilson 2022; de Beurs et al. 2022; Zhao, Ford & Tinney 2022b), while others focus on the spectrum level mitigation (e.g. Davis et al. 2017; Jones et al. 2017; Cretignier et al. 2021; Cretignier, Dumusque & Pepe 2022). For more details on existing activity mitigation techniques, we refer readers to Zhao et al. (2022a) for an overview.

On longer time-scales of several years, the influence of magnetic activity cycles becomes prominent. Solar-type stars exhibit cycles of magnetic activity spanning several years, which can potentially affect all the above activity signals. Such cycles have been linked to long-term RV fluctuations over the years (Dumusque et al. 2011b). This means the RV signals attributed to these cycles can be easily confounded with the RV signals from long-period planets. Meunier, Lagrange & Cuzacq (2019) demonstrated that such effects can be substantially reduced by decorrelating the RV from chromospheric emissions. In addition to the long-term baseline variations, magnetic activity cycles can alter the characteristic period of signals induced by active regions over time. This is because the distribution of active regions across latitudes changes throughout the magnetic activity cycle (e.g. the butterfly diagram of the sun) (e.g. Foing 1988). If the surface rotation rate varies from equator to pole (differential rotation), the rotation period inferred from the modulation of surface heterogeneities (whether in photometry or spectroscopic indicators) will vary along the magnetic cycle. For a sun-like differential rotation and butterfly pattern, the active regions move from higher to lower latitudes as the cycle progresses, and their rotation period decreases.

Since 2003, the high-resolution spectrograph HARPS has been observing thousands of stars. The rich archival, high-quality data from HARPS provides a unique opportunity to test and apply state-of-the-art methods for activity modelling and mitigation. In this paper, we apply the multidimensional Gaussian Process framework to HARPS observations of 268 well-observed targets. We discuss sample selection, data reduction and pre-processing, as well as the basic properties of the sample in Section 2. We then briefly introduce the multidimensional GP framework and detail its implementation in Section 3. We discuss results regarding stellar rotation in Section 4, and facular to spot ratio in Section 5. We summarize our key conclusions and outline future work in Section 6.

2 THE HARPS SAMPLE

2.1 Sample selection

We utilized archived data from the HARPS, accessible via the ESO science archive.[1]

We retrieved all publicly available HARPS spectra using the ESO's `astroquery`[2] (Ginsburg et al. 2019) package. For every observation and each target, we cross-matched the stellar name and position with their respective counterparts in the `simbad` data base (Wenger et al. 2000). This step ensured the removal of potential misclassifications from the ESO archive and close-in binary systems from our data set. Polarimetric data, which only constitute a minor portion of the HARPS archive, have been discarded as they were not reduced automatically by the standard pipeline. We did not implement cuts based on the signal-to-noise ratio (SNR) of the spectra, or cuts based on whether the simultaneous calibration has been applied. We anticipated that these factors would manifest themselves through the uncertainties of the pipeline products, which would be taken into account statistically by our Bayesian framework introduced later. Our preliminary target set included a total of 1438 targets with spectral types spanning from F to M. Their effective temperatures (T_{eff}) approximately ranged between 2800 and 7500 K.

To guarantee a sufficient observation duration for our targets, we excluded those that had less than 40 daily-binned observations. In pursuit of homogeneity in the determination of the stellar parameters, for example effective temperature T_{eff}, surface gravity log g, we restricted our sample to stars listed in the catalogue published in Gomes da Silva et al. (2021), and used the parameters listed in that catalogue throughout our paper. Our final sample contains 268 targets, with spectral types spanning from F to K. Fig. 1 shows

---

[1] http://archive.eso.org/scienceportal/home

[2] https://github.com/astropy/astroquery

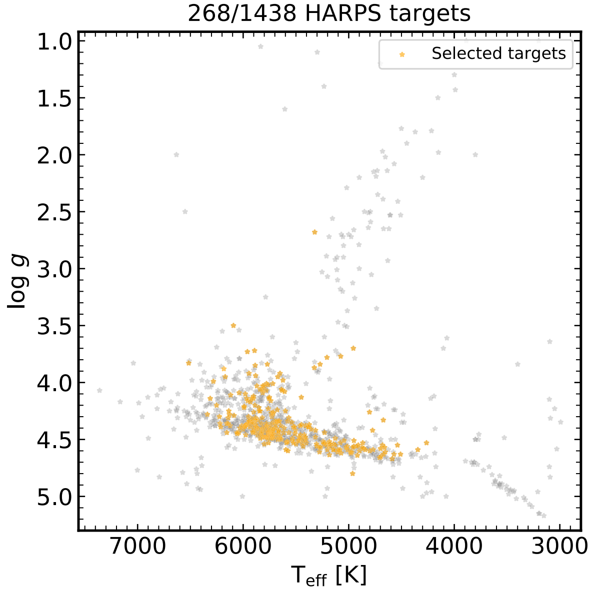

Figure 1. Our sample selection in an HR diagram, with log g versus $T_{\rm eff}$ from *Gaia* DR2 (Gaia Collaboration 2016, 2018). The grey points show the 1438 targets on our initial list. The selected 268 targets in our final sample are highlighted in orange.

our sample selection in an Hertzsprung–Russell (HR) diagram, with log g versus $T_{\rm eff}$ from *Gaia* DR2 (Gaia Collaboration 2016, 2018). The grey points show the 1438 targets on our initial list, while the selected 268 targets in our final sample are highlighted in orange.

2.2 Data reduction and pre-processing

The raw data underwent automatic reduction using version 3.5 and/or 3.8 of the HARPS Data Reduction Software (DRS). For each target, CCFs were computed by correlating the reduced spectra with a line mask that matches the spectral type of the star. CCF proxies, namely RV and Bisector Inverse Slopes (BISs), were then measured from the CCFs within the DRS. Additionally, we computed a chromospheric emission metric, *S*-index, from the Ca II H and K lines (3968.47 and 3933.66 Å, respectively) in the S1D spectra, employing the `ACTIN`[3] (Gomes da Silva et al. 2018) package.

For each time-series, we calculated the median absolute deviation (MAD) metric, which is considered a more reliable measure of statistical dispersion than the often-employed standard deviation, especially in the presence of outliers. Data points exceeding three times the MAD value were identified as outliers and subsequently excluded. Any time-series extending beyond BJD = 2457161.5 was partitioned into two sections for the purpose of outlier removal, given the expectation of two separate baselines resulting from the HARPS fibre upgrade. Finally, we binned each time-series to a maximum of one data point per day.

2.3 Basic properties of the sample

We showcase the basic properties of the 268 targets in our sample using HR diagrams in Fig. 2. The colours of the points in the left, middle, and right panels represent the number of data points in the pre-processed time-series, the mean SNR per pixel (in échelle order 50) of the acquired spectra, and the mean log $R'_{\rm HK}$ of the star, using values from the catalogue provided by Gomes da Silva et al. (2021), respectively. We can see that the numbers of data points in our sample vary, ranging from 40 to over 400, though the majority fall between 40 and 100. The mean SNR spans from 50 to above 300. The mean log $R'_{\rm HK}$ for the majority of the targets are below –4.4, suggesting that they are predominantly inactive stars. This aligns with expectations, given that the primary goal of HARPS is exoplanet detection, leading the survey to prioritize low-activity stars.

In Fig. 3, we show the normalized rms of the time-series for both *S*-index and BIS, plotted against the mean log $R'_{\rm HK}$. The rms values serve as direct metrics of variability in the activity indicators, and as such, they are anticipated to correlate more intimately with the challenges of activity mitigation. We find, however, no clear correlation between the overall rms values and the mean log $R'_{\rm HK}$, even though there appears to be a tentative positive correlation between the rms's upper envelope and the mean log $R'_{\rm HK}$. For instance, at a mean log $R'_{\rm HK}$ value of approximately –4.9, the corresponding rms for either *S*-index or BIS can fluctuate by an order of magnitude. Therefore, we deduce that relying solely on the mean log $R'_{\rm HK}$ is inadequate as an activity metric within the context of activity mitigation. We recommend that future survey target selections consider additional metrics alongside mean log $R'_{\rm HK}$.

3 MODEL FOR STELLAR ACTIVITY

Different processes of stellar activity, for example p-mode oscillations, granulation, active regions, and magnetic activity cycles, can induce variations in the time-series of RV and spectroscopic activity indicators at various time-scales. In this section, we focus on modelling the variations induced by the active regions – notably the effects of faculae/plages and spots. This is primarily because such activity signal is modulated by the rotation of the star, and the associated time-scales (i.e. tens of days) are closest to the orbital periods of the planets. In the following, we introduce the multidimensional GP framework to model such activity-induced signals in Section 3.1, with the aim of measuring the rotation period of the stars. We then detail the implementation of the framework to activity indicators in Section 3.2.

3.1 Multidimensional Gaussian Processes framework

GPs are commonly used in recent years as a tool to model stellar activity, given their ability to model the data by parametrizing its covariance matrix to constrain the characteristics of the data, for example period, evolution time-scale. This avoids the necessity of knowing the exact deterministic form of the underlying physical processes, which can be extremely hard in the case of modelling stellar activity as it is expected to be stochastic. For comprehensive descriptions of GPs, we refer readers to specialized literature, for example Rasmussen & Williams (2006), Roberts et al. (2017) and Aigrain & Foreman-Mackey (2023).

At its core, a GP model is characterized by a mean function and a kernel function, the latter parametrizing the covariance matrix. Parameters within these kernel functions, termed hyper-parameters, shape the characteristics of the modelled data rather than its exact form. For example, a frequent choice for modelling stellar activity is the QP kernel

$$k_{QP}\left(t, t'\right) = A \exp\left[-\Gamma \sin^2\left(\frac{\pi\left(t-t'\right)}{P}\right) - \frac{\left(t-t'\right)^2}{2l^2}\right], \qquad (1)$$

---

[3] https://github.com/gomesdasilva/ACTIN

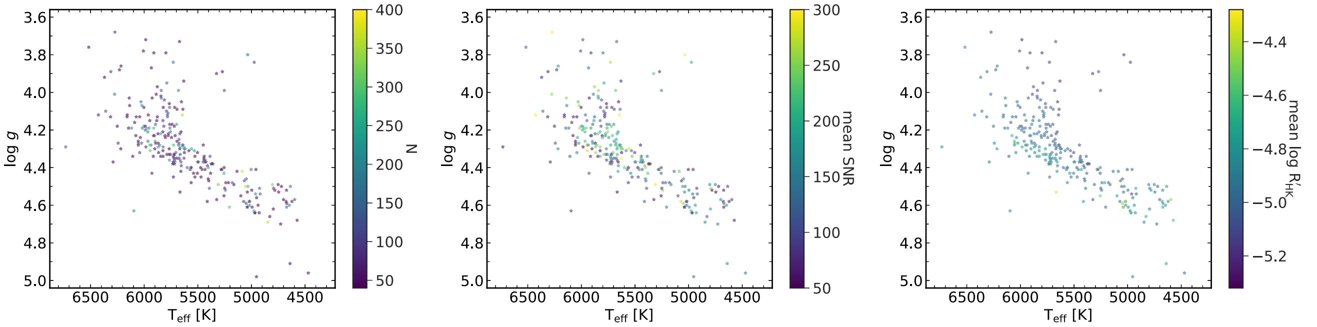

Figure 2. The figure shows the basic properties of the 268 targets in our sample. The targets are displayed in HR diagrams, and the colours of the points in the left, middle, and right panels represent the number of data points in the pre-processed time-series, the mean SNR of the acquired spectra, and the mean log $R'_{\rm HK}$ of the star, respectively.

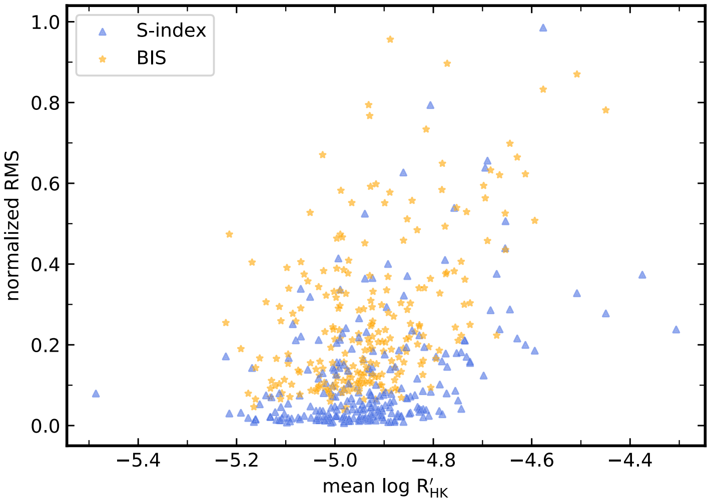

Figure 3. The figure shows the normalized rms of the time-series for both S-index and BIS versus the mean log $R'_{\rm HK}$.

where A is the amplitude representing the overall scale of the variation from the mean function, P is the characteristic period of the variation, Γ is the harmonic complexity, which in simpler terms indicates how much the variation strays from a pure sine oscillation within a given period. l is the 'evolution time-scale', which scales with the maximum distance of two data points that are strongly correlated.

Aiming to maximize the usage of information from the spectroscopic time-series in modelling the stellar activity, we want to model the activity signals from the RVs together with a set of selected spectroscopic activity indicators, that is, S-index and BIS. Following Aigrain et al. (2012); Rajpaul et al. (2015); Barragán et al. (2022); Delisle et al. (2022), we assume a set of N observable time-series, $Y_{i=1,...,N}(t)$, which can be time-series of RV and activity indicators, and each time-series Y_i follows

$$Y_i(t) = f_i(t) + [a_i G(t) + b_i \dot{G}(t)] + \epsilon_i(t), \tag{2}$$

where $f_i(t)$ is the deterministic part of the model. For RV, it is where the mean function and planet-induced RV are incorporated. For activity indicators, it is simply the mean function. $\epsilon_i(t)$ is the measurement'white' noise, which normally includes photon noise, calibration noise, etc. Every $Y_i(t)$ has a shared entity, $G(t)$. We interpret this as a latent GP variable, approximating the proportion of the visible stellar disc blanketed by active regions. Commonly, a GP with a QP kernel is the modelling choice for this variable. $\dot{G}(t)$ is the first temporal derivative of $G(t)$ and remains a GP, roughly representing how the active regions evolve in time on the stellar disc. Coefficients a_i and b_i are free parameters that harmonize the interplay between the latent GP variables, G and $\dot{G}$, and various observable time-series, Y_i.

Building on this framework, a fully parametrized covariance matrix $\mathbf{K}$ for the N time-series $Y_{i=1,...,N}(t)$ can be established. With a known mean function $\mathbf{m}$ and covariance matrix $\mathbf{K}$, the likelihood function can be written in analytic expression as

$$\mathcal{L} = \frac{1}{\sqrt{2\pi\,|\mathbf{K}|}} \exp\left(-\frac{1}{2}(\mathbf{y}-\mathbf{m})^{\rm T}\mathbf{K}^{-1}(\mathbf{y}-\mathbf{m})\right), \tag{3}$$

where $\mathbf{y}$ encompasses the vector of N observed time-series $Y_i(t)$. Full Bayesian frameworks, such as Monte Carlo Markov Chain (MCMC) or nested sampling, can be implemented with $\mathcal{L}$ to explore the posterior distributions of free parameters in the model. We direct readers to Rajpaul et al. (2015) and Barragán et al. (2022) for details.

For $G(t)$, the traditional approach involving a QP kernel, as outlined in equation (1), faces the drawback of computational costs that rise cubically in relation to the size of the data set. An alternative option is to use a fast approximated kernel, such as a Matern 3/2 exponential periodic (MEP) kernel facilitated in `S + LEAF 2`[4] (Delisle et al. 2022), of which the computational cost only scales linearly. Such efficiency becomes indispensable when tasked with

---

[4] https://gitlab.unige.ch/Jean-Baptiste.Delisle/spleaf

Table 1. Priors and inferred value of selected parameters in the model for the example on the ∗ 61 Vir (HD 115617) data set.

Parameter	Prior *	Inferred value
Period P (d)	$\mathcal{U}[0.1, 60.0]$	$32.1^{+0.2}_{-0.2}$
Evolution timescale l (d)	$\mathcal{U}[1, 5000]$	186^{+78}_{-50}
Harmonic complexity Γ	$\mathcal{U}[0.01, 5.00]$	$0.68^{+0.16}_{-0.12}$
$a_{\mathrm{BIS}}(\mathrm{m\ s^{-1}})$	$\mathcal{U}[-\mathrm{rms(BIS)}, \mathrm{rms(BIS)}]$	$0.55^{+0.15}_{-0.08}$
$b_{\mathrm{BIS}}(\mathrm{m\ s^{-1}\ d^{-1}})$	$\mathcal{U}[-10 * \mathrm{rms(BIS)}, 10 * \mathrm{rms(BIS)}]$	$-3.5^{+0.7}_{-0.9}$
$a_{S\text{-index}}(\mathrm{d^{-1}})$	$\mathcal{U}[-\mathrm{rms(S-index)}, \mathrm{rms(S-index)}]$	$0.0013^{+0.0003}_{-0.0002}$

Note. * $\mathcal{U}$[a, b] refers to a uniform prior between a and b.

analysing expansive data sets for a large volume of targets without straining computational resources. We refer readers to Delisle et al. (2022) for details on the MEP kernel.

3.2 Implementation

We implemented the multidimensional GP framework on every target in our sample. As we initially focused on the activity indicators in the present work, the exact form of the framework we used can be outlined as follows

$$\begin{aligned} \mathrm{BIS}(t) &= f_{\mathrm{BIS}}(t) + a_{\mathrm{BIS}}G(t) + b_{\mathrm{BIS}}\dot{G}(t) + \epsilon_{\mathrm{BIS}}(t), \\ S\mathrm{-index}(t) &= f_{S\mathrm{-index}}(t) + a_{S\mathrm{-index}}G(t) + \epsilon_{S\mathrm{-index}}(t), \end{aligned} \tag{4}$$

where

$$\begin{aligned} f_{\mathrm{BIS}}(t) &= \overline{\mathrm{BIS}(t)}, \\ f_{S\mathrm{-index}}(t) &= \overline{S\mathrm{-index}(t)}, \end{aligned} \tag{5}$$

and $\epsilon(t)$ are white noise models containing measurement noise and jitter terms. BIS is proved to be interlinked with both $G(t)$ and its derivative $\dot{G}(t)$, while S-index is exclusively related to $G(t)$ (e.g. Isaacson & Fischer 2010; Dumusque, Boisse & Santos 2014; Thompson et al. 2017). Hence we exclude $\dot{G}(t)$ term for S-index. In terms of choices of kernels for $G(t)$, we opted for MEP kernels available in `S + LEAF` introduced earlier, which is a faster approximation of the QP kernel. To explore the posterior of free parameters, we used nested sampling through `PolyChord`[5] (Handley, Hobson & Lasenby 2015a, b), with all priors on the free parameters set as uninformative. This nested sampling approach is favoured here as it demonstrates better performance when compared to MCMC approaches, especially in data sets exhibiting multimodality.

We show an example of implementing the framework using the ∗ 61 Vir data set. In Table 1, we show the inferred values of the free parameters in the model based on the posterior distributions, alongside the priors designated for the parameters during the sampling. The inferred values are the median of the posterior distributions, and the statistical uncertainties are given by the 16th to 84th percentile range.

Fig. 4 shows a multidimensional GP fits to the time-series of ∗ 61 Vir (HD 115617) data set. In the left panel, the black markers show the time-series of S-index and BIS, and their associated uncertainties. The coloured (blue and coral) lines show the GP predictions over the observations, and the corresponding shaded areas of the lines show one σ uncertainty of predicted distributions. The horizontal dashed-grey lines show the means of the time-series. The grey extensions on the errorbars show the jitter terms. The right panel show posterior distributions of selected model parameters, including period, evolution time-scale, and harmonic complexity.

4 STELLAR ROTATION

4.1 Rotation period measurement

The variations induced by active regions in activity indicators, modulated by the rotation of the star, are believed to closely represent the star's true rotation period (e.g. Angus et al. 2018; Nicholson & Aigrain 2022). As such, the rotation period is captured by the hyper-parameter'period' in our multidimensional GP model when the activity-induced signal is well modelled.

We applied the multidimensional GP framework with a MEP kernel to each star in our sample. To determine whether the period is securely detected, on a separate analysis, we applied the same framework but used a Matern 3/2 kernel instead with GP, representing an aperiodic model in comparison to the above periodic model (with the MEP kernel). The evidence Z of each model is estimated through nested sampling to calculate $\Delta\ln \mathrm{Z} = \ln \mathrm{Z}_{\mathrm{periodic}} - \ln \mathrm{Z}_{\mathrm{aperiodic}}$. A positive value indicated that the periodic model is preferred. We then used $\Delta\ln \mathrm{Z}$ as our starting criterion to select targets where the periodic model is preferred. Additionally, we rejected cases through visual inspection where the $\Delta\ln \mathrm{Z}$ was unreliable because of two possible scenarios. First, in cases where neither model fits well, the $\Delta\ln \mathrm{Z}$ criterion could be biased as the Bayesian model comparison is only meaningful when both models adequately fit the data. Secondly, the MEP kernel (or the QP kernel in general) we employed has regions in the parameter space that could behave aperiodically. In such cases, even if the periodic model appears preferable based on evidence difference, secure detection of the period is not guaranteed. Upon thorough vetting, we identified 49 targets for which we believe the model adequately captured the activity-induced variations, resulting in an accurate recovery of their true rotation periods.

We also want to emphasize that in comparison to conventional methods, such as periodograms or the autocorrelation function (ACF), the GP approach displays greater resilience against harmonic misdetection when determining rotation periods (e.g. Angus et al. 2018). This robustness arises from the utilization of the MEP or QP kernel, where potential harmonic components are inherently considered, that is, the 'harmonic complexity' hyperparameter serves as an approximate gauge of the harmonic contribution. This ensures the algorithm finds the true rotation period which is associated with the lowest base frequency.

The selected 49 targets are shown in an HR diagram in Fig. 5, with the colour of the markers representing their recovered rotation periods. All other targets of which the periods have not been successfully recovered are denoted with grey markers. The dotted line at log g = 4.1 approximately separates main-sequence stars from evolved stars, that is, sub-giants. Notably, we find that the rotation period broadly decreases as effective temperature rises (or for earlier spectral types), although there is a considerable amount of scatter at

---

[5] https://github.com/PolyChord/PolyChordLite

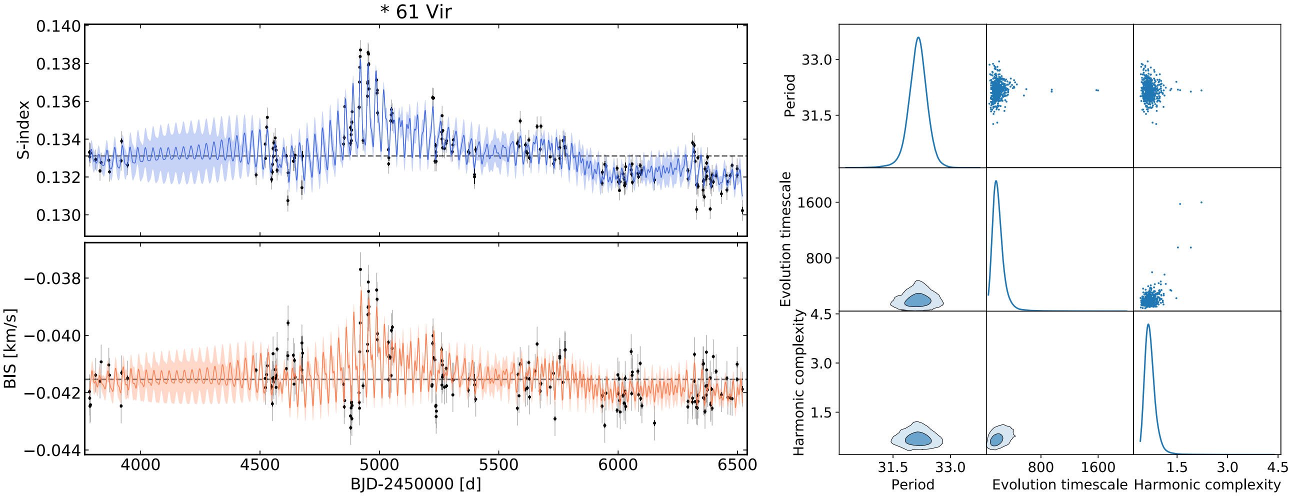

Figure 4. Demonstration of multidimensional GP fit on the $*$ 61 Vir (HD 115617) data set. In the left panel, the black markers show the time-series of *S*-index and BIS, and their associated uncertainties. The coloured (blue and coral) lines show the GP predictions over the observations, and the corresponding shaded areas of the lines show one σ uncertainty of predicted distributions. The horizontal dashed grey lines show the means of the time-series. The grey extensions on the errorbars show the jitter terms. The right panel show posterior distributions of selected model parameters, including period, evolution time-scale and harmonic complexity.

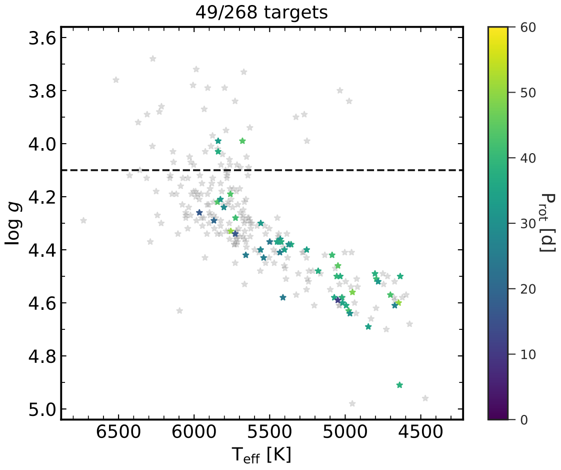

Figure 5. HR diagram of our sample with the coloured points showing the measured rotation period for the 49 targets which passed our vetting procedure. The grey markers denote the other targets for which the rotation periods were not recovered or were not considered sufficiently robust to include in subsequent analysis. The dotted line at log g = 4.1 approximately separates main-sequence stars from evolved stars, that is, sub-giants.

any given temperature. This is broadly consistent with both theoretical expectations (e.g. Skumanich 1972) and preceding rotation period surveys (e.g. McQuillan, Mazeh & Aigrain 2014). Further insights on age–activity–rotation relations are discussed in Section 4.3.

Regarding the detection rate, there are approximately 23 per cent of main-sequence G and K stars of which the rotation period is well recovered. However, this rate decreases significantly for earlier type stars such as F stars, and for sub-giants. The rapid rotation of F stars, typically with periods under 10 d, necessitates denser time sampling than what is currently available to accurately determine their rotation periods. In the case of sub-giants, their evolving nature results in diminished or altered activity patterns, deviating from the assumption of our activity model and thus reducing the detection rate. It is important to note that the detection rate for the rotation period can be considered as an indirect measure of the model's efficacy at mitigating activity signals across different stellar types. In this context, the model demonstrates the best performance for G and K stars. For F stars, the model's efficacy could be enhanced with optimized sampling, tailored to capture their rapid rotation. However, it is essential to recognize that effective activity modelling does not necessarily equate to a target's appropriateness for planet detection. For example, challenges in modelling activity could arise due to a lack of pronounced active regions on the stellar surface. In such cases, the amplitude of the activity signal remains minimal and as such the star could still possibly be an attractive candidate for exoplanet detection.

Last but not least, it is important to highlight that compared to traditional methods like the Lomb–Scargle periodogram, the GP method holds an advantage in determining the signal's period when the rotational modulation signal evolves over time (Angus et al. 2018). Additionally, with the multiGP method used in this work, we search for and identify common periodic signatures among multiple time-series, thereby increasing the confidence in the measured rotation period. Moreover, the multiGP framework offers insights beyond just the rotation periods of the stars. Specifically, it provides a quantitative understanding of the covariance structure of the activity signals. Such information can be integrated into statistical frameworks to disentangle activity from planetary signals in the RVs. This can be achieved through either simple linear regression models, or a more complex framework that explicitly takes the covariance structure into account, such as the L1 periodogram of Hara et al. (2017). We defer further exploration of this potential to future work.

4.2 Rossby number

The Rossby number Ro, which is given by the ratio of the rotation period P_{rot} to the convective turnover time-scale τ_{c}

$$\mathrm{Ro} = \mathrm{P}_{\mathrm{rot}}/\tau_{\mathrm{c}} \tag{6}$$

is a key parameter of the dynamo process that gives rise to large-scale magnetic fields among the stars we are considering in this study. Numerous empirical studies have shown that Ro is a key parameter

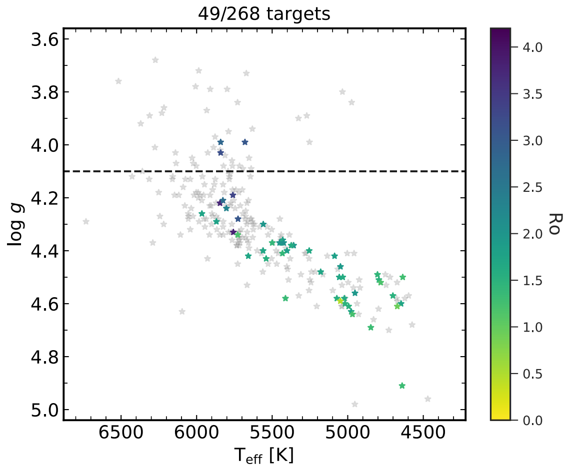

Figure 6. As Fig. 5, but the colour scale now shows the Rossby number.

for the angular momentum evolution, as well as for magnetic field strength and topography of late-type stars (see e.g. Noyes et al. 1984). To first order, it is an indicator of the activity level of the star: the lower the Rossby number, the more active the star.

We evaluated the Rossby number for the stars in our sample with rotation period measurements, using the empirical relations from Cranmer & Saar (2011) to calculate $\tau_{\rm c}$

$$\tau_{\rm c}\,(T_{\rm eff}) = 314.24 \exp\left[-\left(\frac{T_{\rm eff}}{1952.5\ {\rm K}}\right) - \left(\frac{T_{\rm eff}}{6250\ {\rm K}}\right)^{18}\right] + 0.002. \tag{7}$$

The Rossby number of the sample is shown in the right panel of Fig. 6. The coloured points show the selected 49 targets from the visual vetting. Most of the stars in our sample have a relatively high Rossby number, that is, Ro > 1.0, and are thus inactive stars. This is unsurprising, as most archival HARPS observations were taken as part of planet surveys, which tend to avoid active stars. Unlike $\log R'_{\rm HK}$, the correlation between the Rossby number and the effective temperature is relatively weak, and can be explained mostly by the fact that the hotter stars in our sample are starting to evolve off the main sequence.

4.3 Implications for spin-down of middle-aged stars

Sun-like stars are expected to undergo spin-down following a simple power law (e.g. Skumanich 1972) to the first order during their main-sequence stage. This spin-down emerges from the continuous loss of angular momentum, a consequence of torques generated from interactions between the star's surface magnetic field and its stellar wind. However, subsequent observations from open clusters spanning a wide age range challenged the Skumanich-like spin-down. Specifically, these results have brought to light two phases in a star's evolution where the spin-down process appears to 'stall' (Meibom, Mathieu & Stassun 2009; Agüeros et al. 2018; Douglas et al. 2019).

To account for these stalling effects, several scenarios have been proposed. The two main hypotheses are the core-envelope coupling (e.g. Spada et al. 2011; Lanzafame & Spada 2015; Spada & Lanzafame 2020; Johnstone, Bartel & Güdel 2021) happening at a few Myrs to a Gyr, and the weakened magnetic breaking (e.g. van Saders et al. 2016) happening at a few Gyrs. The former suggests angular momentum can be transferred from the radiative core to the convective envelope due to internal differential rotation, attenuating the spin-down of the envelope. The latter indicates that magnetic braking is substantially weakened once the star achieves a critical Rossby number, possibly due to a change in the magnetic field's morphology. This alteration – shifting from a dipole field to a quadrupole field or an even more intricate configuration – makes it less effective at shedding angular momentum (Réville et al. 2015).

Gaps in the rotation period versus effective temperature diagram have been found with Kepler stars (e.g. McQuillan, Aigrain & Mazeh 2013; McQuillan et al. 2014; Gordon et al. 2021). These gaps can potentially be explained by the aforementioned stalling effects. David et al. (2022) provide stronger evidence by combining the *Kepler* rotation periods with more accurate spectroscopic effective temperatures from, for example the Large Sky Area Multi-Object Fiber Spectroscopic Telescope (LAMOST) (Cui et al. 2012; Zhao et al. 2012). Their findings indicate two prominent pile-ups in the period-effective temperature diagram. The short-period pile-up is attributed to the core-envelope coupling mechanism, while the long-period pile-up is linked to the phenomenon of weakened magnetic braking. This latter association is primarily because it aligns seamlessly with a consistent Rossby number curve.

We constructed a similar diagram, by combining rotation periods measured in *Kepler* data by McQuillan et al. (2014) with effective temperatures from LAMOST. This resulted in a blue Kernel Density Estimation (KDE) plot, displayed in the background of Fig. 7, generated with the codes[6] provided by David et al. (2022). Empirical cluster sequences of different ages are shown in grey lines, derived from Curtis et al. (2020). The purple lines correspond to constant Rossby numbers, following

$$P_{\rm rot}\,({\rm Ro}, {\rm T}_{\rm eff}) = {\rm Ro} \times \tau_{\rm c}\,({\rm T}_{\rm eff})\,, \tag{8}$$

with convective turnover time-scales from Cranmer & Saar (2011) as equation (7).

In the KDE, the long-period pile-up is visible below the Ro = 1.45 curve, while the short-period pile-up appears above the Ro = 0.4 curve. The Sun is shown as a reference in red, with $T_{\rm eff,\odot} = 5772$ K (Prša et al. 2016) and $P_{\rm rot,\odot} = 27 \pm 2$ d estimated from Snodgrass & Ulrich (1990). We have overlaid the asteroseismic sample from Hall et al. (2021), depicted in grey, and our HARPS sample of 49 well-determined rotation periods (detailed in Section 4.1) in orange. Both samples clearly occupy a distinct period-temperature space to the much larger *Kepler*, predominantly located above the long-period pile-up. We interpret this primarily as a consequence of the different selection effects for the three samples. The *Kepler* sample, while much larger and benefiting from tight, regular time sampling, relies on detecting the rotational modulation of active regions in broad-band optical light curves. This becomes increasingly difficult for less active stars as the fraction of the stellar disc covered by active regions drops, and for slower rotators as the rotation period becomes comparable to both the lifetime of the active regions and the duration of individual *Kepler* 'quarters'. The asteroseismic sample uses *p*-modes to measure internal and surface rotation rates, and is strongly biased towards hotter and lower gravity (evolved) stars, for which the amplitude of the *p*-modes is larger and their frequencies lower than for later type main-sequence stars. The HARPS sample spans a longer baseline and uses spectroscopic activity indicators rather than broad-band photometry to detect the rotational modulation of active regions. It is reasonable to expect that targetted indicators should

---

[6] https://github.com/trevordavid/rossby-ridge

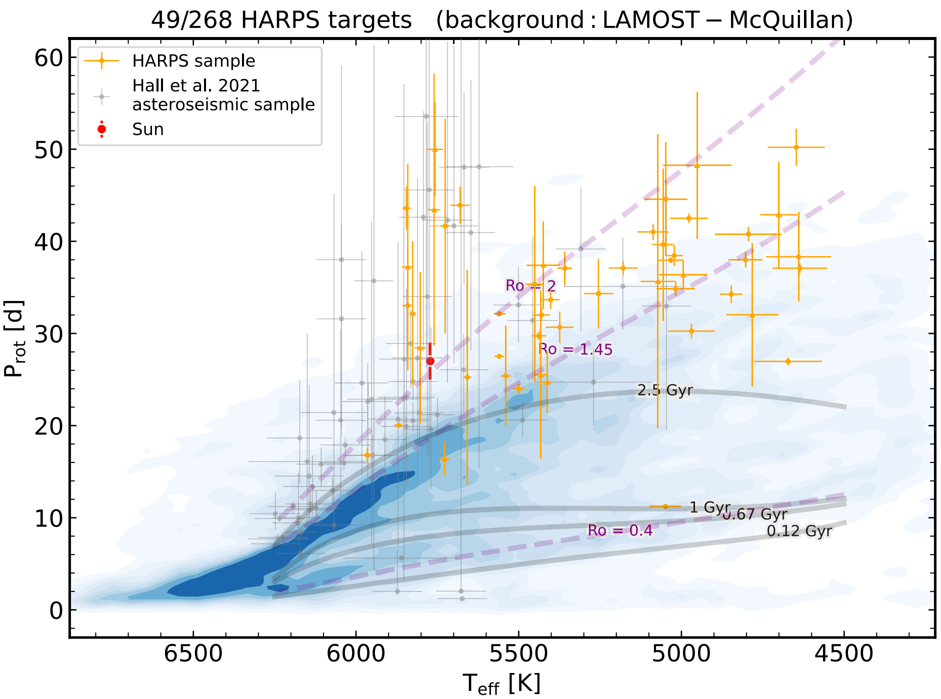

Figure 7. Rotation period versus effective temperature for our sample, compared to previous results from the literature. The blue shading in the background represents a kernel density estimate of the *Kepler*/LAMOST period-temperature results. Empirical cluster sequences of different ages are shown in grey lines, derived from Curtis et al. (2020). Lines of constant Rossby number are shown in purple. The asteroseismic sample of Hall et al. (2021) is plotted in grey and our new results based on HARPS data are plotted in orange.

be more sensitive to active regions than photometry, particularly as the active regions decrease in size and number and the rotation slows. A possible additional contributing factor is the fact that, while dark spots dominate the activity patterns for active stars, less active stars tend to be more faculae-dominated (Meunier et al. 2010). The photometric signatures of faculae are rather subtle, whereas they have strong chromospheric signatures, which are probed by spectroscopic indicators such as $\log R'_{\rm HK}$ and also have a strong signature in line-shape indicators such as the BIS via their local dampening effect on convective flows. A more in-depth discussion on this topic can be found in Section 5.

Considering the combined HARPS and asteroseismic samples, we see that two distinct populations emerge. The first is composed of hotter stars (with $T_{\rm eff} \geq 5700$ K), mostly from the asteroseismic sample, though with a handful of HARPS measurements. This population follows a very steep period–temperature relation, consistent with the rapid spin-down expected as stars leave the main sequence and start to evolve towards the red giant branch.

The second population, predominantly from our sample, consists of cooler (mid-G to mid-K) main-sequence stars. It follows a shallower period-temperature relation, and its upper envelope corresponds to the Ro = 2 curve. This second population could possibly be the extension of the long-period pile-up observed in the *Kepler* sample, but skewed towards cooler stars. In the *Kepler* sample, the long-period pile-up is less pronounced at cooler temperatures, but this could be a selection effect: at lower temperatures, the pile-up moves to longer periods, which correspond to lower photometric amplitudes, and the stars also become intrinsically fainter. In Fig. 8, we show the Rossby numbers computed for our sample compared to the KDE of the *Kepler* sample. They fall in the range of 1.5–2.5, consistent with the critical Rossby number inferred from the photometric long-period pile-up. A slight discrepancy between this tail and the anticipated long-period pile-up extension might arise from biases in effective temperature measurements from different sources, as argued in David et al. (2022) in the context of the asteroseismic sample.

5 FACULAE-TO-SPOTS RATIO

Spots and faculae (or their chromospheric counterpart, plages) are the two main types of active regions that are expected to induce variations in the RVs and activity indicators used in planet searches. These variations are induced by two simultaneous processes. The first, known as the photometric effect, is thought to be mainly induced by dark spots, which locally reduce (or even suppress entirely) the local flux emerging from the stellar surface. The other is due to the fact that convective up-flows are suppressed in regions of enhanced magnetic flux density, which includes both spots and faculae. This results in a local reduction in the net blue-shift caused by convective flows relative to the 'clear' photosphere, known as the Inhibition of Convective Blueshift (ICB) effect. Both processes cause distortions to the disc-integrated line profiles, resulting in variations the RV, FWHM, and BIS, while chromospheric activity indicators such as the S-index or $\log R'_{\rm HK}$ are sensitive to the fractional coverage of the active regions themselves.

The differentiating factor between spots and faculae lies in the processes through which they induce variations. While spots cause variations via both these processes, faculae primarily influence the ICB effect (e.g. Dumusque et al. 2014). Within the context of our multidimensional GP framework, the terms $aG(t)$ and $b\dot{G}(t)$ distinctively represent these two effects (e.g. Aigrain et al. 2012; Rajpaul et al. 2015). Hence, the ratio of the rms values of these two terms, RMS[$aG(t)$] RMS[$b\dot{G}(t)$], which we denote as A/B in the following text, can be interpreted as an approximate representation

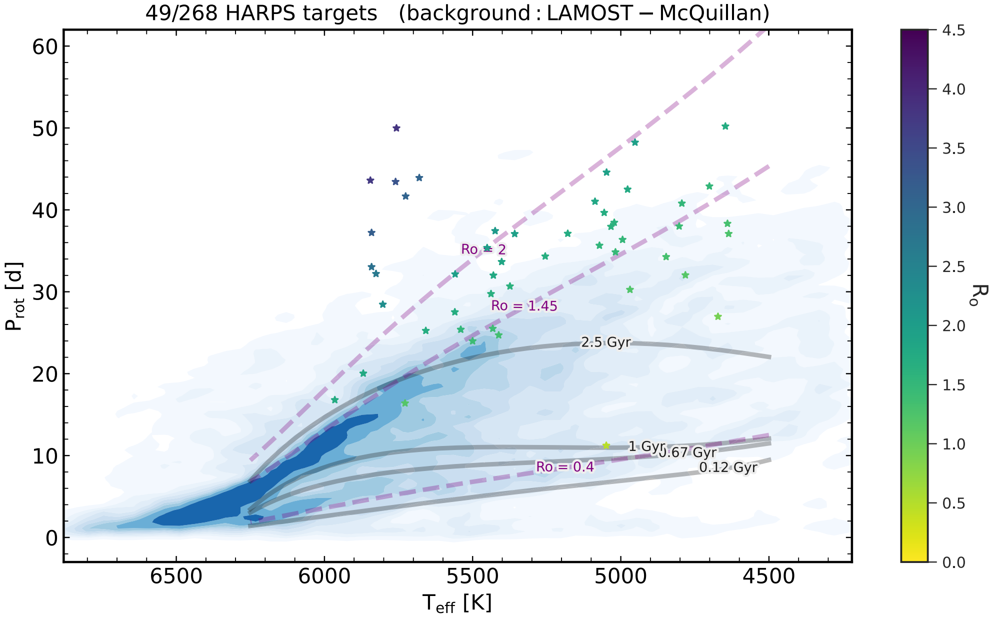

Figure 8. As Fig. 7, but the points now show our sample colour-coded according to Rossby number.

of the relative faculae-to-spots ratio. This potentially offers an interesting way to measure the faculae-to-spots ratio in the sample of stars where we consider the results of the GP modelling to be sufficiently robust.

In turn, doing this would allow us, in principle, to test the widely held paradigm that more magnetically active stars are more spot-dominated, while quieter stars have fewer spots and more faculae (e.g. Meunier et al. 2010; Amazo-Gómez et al. 2020). Of course, direct measurements of the star's magnetic field necessitate polarimetric observations, and few stars in our sample have such observations. However, the Rossby number Ro derived in Section 4.2 is known to correlate strongly with the strength of the magnetic field $< \mathrm{B} >$ (e.g. Reiners, Schüssler & Passegger 2014; Vidotto et al. 2014; Reiners et al. 2022), with an exception for very inactive stars (i.e. $\mathrm{Ro} > 2$).

For the targets of which we have detected their rotation periods securely, we examined the relationship between the rms ratio A/B and the derived Rossby number Ro in the left panel of Fig. 9. The error bars show the propagated statistical uncertainties, and the colour scheme indicates the effective temperature of the stars. We excluded samples exhibiting uncertainties in the A/B exceeding 200 per cent.

To evaluate the monotonic relationship between the A/B and the Ro, we calculated the Spearman correlation coefficient, considering an upper cut-off value for Ro in the range of 1.6–4.0. The result is shown in the right panel of Fig. 9. We found that the Spearman coefficient peaks between $1.8 < \mathrm{Ro} < 2.0$ with a value of 0.62, after which the value drops rapidly. In addition, we conducted linear fits to $\log(A/B)$ as a function of Ro, and showed the slope of the fit versus the Ro cut-off value in the same panel. We found that the slope also peaks between $1.8 < \mathrm{Ro} < 2.0$, behaving similarly to the Spearman coefficient. Both proxies indicate a relatively strong positive correlation between A/B and Ro until $\mathrm{Ro} \approx 1.9$, after which the correlation significantly weakens.

Additionally, we conducted analyses to assess the impact of the data point at $\mathrm{Ro} \approx 0.5$ by excluding it from the correlation analysis. The results are represented as thinner lines in the same panel, labelled as $\mathrm{Ro} > 0.6$. Both the Spearman coefficient and the slope showed behaviours remarkably similar to those observed in the full analysis. This similarity suggests that the overall results are not predominantly influenced by this single data point. Despite this, we assert that the detection at $\mathrm{Ro} \approx 0.5$ is robust. The lack of data in the $0.5 < \mathrm{Ro} < 1.0$ range is likely attributed to the HARPS sample's bias towards inactive stars.

The relationship between A/B and Ro is aligned with theoretical predictions: a lower Ro implies a stronger magnetic field and consequently, a star that is more spot-dominated. This leads to a decreased facular-to-spot ratio, mirrored by a lower A/B, which is exactly the trend we have seen in the $\mathrm{Ro} < 1.9$ regime. However, when $\mathrm{Ro} > 1.9$, the correlation disappears, and there is no longer any obvious relationship between the A/B and the Rossby number. We speculate that the disappearance of the correlation might arise from a morphological transition in the stellar magnetic field beyond $\mathrm{Ro} \approx 1.9$, away from a predominantly dipolar configuration. If the B-field structure becomes more complex, the correlation between B-field strength and Rossby number would not be expected to persist.

Intriguingly, the Rossby number at which the correlation with the A/B disappears, $\mathrm{Ro} \approx 1.9$, is close to the Ro that marks the upper envelope of the *Kepler* main-sequence rotation period-temperature distribution in Figs 7 and 8. It also corresponds approximately to the critical Rossby number in the range $1.4 \leq \mathrm{Ro} \leq 2.0$ postulated in stellar spin-down theories (e.g. van Saders et al. 2016; van Saders, Pinsonneault & Barbieri 2019; David et al. 2022), where the efficiency of stellar angular momentum dissipation is expected to drop significantly due to the same alterations in magnetic field morphology.

A more detailed investigation of the faculae-to-spot ratio and its dependence on magnetic field strength would certainly be valuable, but would likely require more sophisticated activity indicators that can help disentangle the contributions of the different types of active regions (see e.g. Crétignier, Pietrow & Aigrain 2024) as well as a larger sample of stars with direct, polarimetric magnetic field measurements, and is therefore beyond the scope of this work.

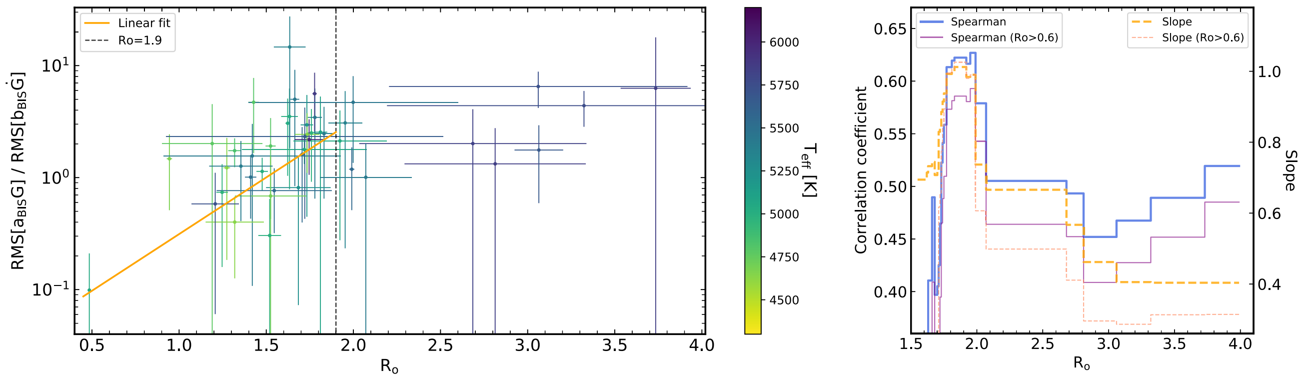

Figure 9. The left panel shows the rms ratio *A*/*B* (a proxy for the faculae-to-spot ratio) versus the Rossby number Ro (more magnetically active stars have smaller Ro). The error bars show the derived statistical uncertainties, and the colour scheme indicates the effective temperature. The dotted grey line indicates Ro = 1.9, and the orange line shows the linear fit to the data within the range of Ro < 1.9. The right panel shows the estimated Spearman correlation coefficient between *A*/*B* and Ro, as well as the slope of the linear fit to log(A/B) as a function of Ro. The two proxies are plotted against the cut-off value of Ro ranging from 1.6 to 4.1. The blue and orange lines show the analysis of the full data, while the thinner purple and coral lines show the analysis excluding the data point at Ro ≈ 0.5 for comparison.

6 CONCLUSIONS

This paper presents the first results from an ongoing study of the activity properties of F, G, and K stars using archival HARPS data. We applied the multidimensional GP framework developed by Rajpaul et al. (2015) and Barragán et al. (2022) for activity mitigation in RV planet searches to activity indicators extracted from HARPS spectra of 268 well-observed targets with precisely determined stellar parameters. Applying the GP framework to such a large data set was made possible by using the efficient implementation of our framework provided by Delisle et al. (2022). While we do plan to perform a joint analysis of the activity indicators and the RVs in the future, this is made challenging by the presence in the RV time-series of residual systematic effects and an unknown number of planetary signals. A new version of the HARPS DRS is under development (Dumusque et al. priv. comm.), which is expected to lead to significantly reduced systematics and has already allowed new planet candidates to be identified (with further HARPS observations being gathered to confirm them, ESO programme 1110.C–4043, PI Hara). In the mean time, applying the multidimensional GP framework to the activity indicators alone already reveals a wealth of useful information. Our key findings are as follows.

We successfully recovered rotation periods for 49 slow rotators in our sample. We found that the rotation period decreases as effective temperature rises, i.e. for earlier spectral types, which is broadly consistent with both theoretical expectations (e.g. Skumanich 1972) and preceding rotation period surveys (e.g. McQuillan et al. 2014). One limitation of our approach is that we do not consider the effects of differential rotation, primarily due to the sparse sampling of the majority of the targets in our sample. A possible extension of this work would be to analyse the data season by season and investigate seasonal variations in the period as well as in the other parameters of the model.

We placed our results in the context of existing, photometric estimates of field star rotation periods from *Kepler*, and discussed their implications for the age–activity–rotation relations of F, G, and K stars. Our samples typically have longer periods than those derived from photometry, with the exception of the asteroseismic sample. We ascribe this to two factors. First, spectroscopic surveys like HARPS have a much longer baseline compared to photometric surveys. This allows for multiseasonal monitoring, increasing sensitivity to slow rotators. Secondly, spectroscopic indicators are more sensitive to active regions, particularly the faculae that tend to dominate in slowly rotating, magnetically inactive stars, than broad-band optical photometry.

Taken together with the pre-existing asteroseismic sample, our new sample of slowly rotating ($P > \approx 30$ d) FGK stars consists of two, distinct sub-populations. One is a potential extension of the long-period pileup towards cooler stars, with Rossby numbers in the range 1.4 < Ro < 2.0. The other consists of ‘hot slow rotators’ with $T_{\rm eff} > 5700$ K which we interpret as sub-giants which are rapidly spinning down as they start to expand.

Overall, our results broadly agree with the findings of David et al. (2022), but this is the first time that the population of late G and K-type slow rotators is observed so clearly, above the ‘critical’ Rossby number of Ro ≈ 1.5 that marks the upper envelope of the period-temperature distributions for *Kepler* stars with photometrically derived surface rotation periods. We infer that angular momentum loss via a magnetised wind continues beyond this critical value, which instead marks the point where the active region covering fraction becomes too low to allow for photometric rotation period estimates.

We also explored indirectly how the ratio of faculae to spots in active regions varies across our sample, using the RMS ratio of $aG(t)$ to $b\dot{G}(t)$ as a proxy. We find that this ratio is positively correlated with the Rossby number up to Ro ≈ 1.9, in accordance with theoretical expectations, since a lower Ro implies a stronger magnetic field and consequently, a more spot-dominated star. The correlation disappears for larger values of Ro, indicating a possible transition in the stars’ magnetic field morphology away from large-scale, predominantly dipolar fields that give rise to clearly detectable rotational modulation in the activity indicators.

Thus, both our rotation period measurements and the relative contribution of higher-order versus lower-order behaviour in the activity indicator time-series are consistent with the idea that a significant transition in magnetic field morphology occurs around a critical Rossby number in the range $1.4 \le \mathrm{Ro} \le 2.0$. Notably, this transition aligns well with the critical Ro values suggested in stellar spin-down theories.

This paper demonstrates that rich information can be extracted from spectroscopic activity indicators, which sheds light on the structure and evolution of stars. Our intention is to extend this methodology to the RV once there is existing progress on the systemic correction and strategy for a thorough search of planetary signals. We note that the covariance structure of the activity signals learnt from this work can be effectively used to separate stellar and planetary components in the RVs.

The longer-term behaviour of the activity indicators analysed in this work can also be used to search for activity cycles in our targets. This will be the topic of the next paper in our series (Crétignier et al. in preparation). In the longer term, we also plan to incorporate the RV time-series, as well as other activity indicators, into our modelling, in order to improve our understanding of the strengths and limitations of the multidimensional GP framework for activity mitigation in RV planet searches, as a function of the stellar properties.

ACKNOWLEDGEMENTS

HY, SA, BK, OB, and NKOS acknowledge funding from the European Research Council under the European Union's Horizon 2020 research and innovation programme (grant agreement no. 865624, GPRV). NKOS thanks the LSSTC Data Science Fellowship Programme, which is funded by LSSTC, NSF Cybertraining grant number 1829740, the Brinson Foundation, and the Moore Foundation; her participation in the programme has benefited this work. MC acknowledges the SNSF support under grant number P500PT_211024. Based on observations made with ESO Telescopes at the La Silla Paranal Observatory under the HARPS Guaranteed Time Observations (GTO) programme. This research has made use of the SIMBAD data base operated at CDS, Strasbourg (France).

7 DATA AVAILABILITY

This work was based entirely on publicly available data download from the ESO archive. Tables and are available in electronic format.

REFERENCES

Agüeros M. A. et al., 2018, ApJ, 862, L33

Aigrain S., Foreman-Mackey D., 2023, ARA&A, 61, 329

Aigrain S., Pont F., Zucker S., 2012, MNRAS, 419, 3147

Amazo-Gómez E. M., Shapiro A. I., Solanki S. K., Kopp G., Oshagh M., Reinhold T., Reiners A., 2020, A&A, 642, 225

Angus R., Morton T., Aigrain S., Foreman-Mackey D., Rajpaul V., 2018, MNRAS, 474, 2094

Arentoft T. et al., 2008, ApJ, 687, L1180

Barragán O., Aigrain S., Rajpaul V. M., Zicher N., 2022, MNRAS, 509, 866

de Beurs Z. L. et al., 2022, AJ, 164, 49

Cegla H., 2019, Geosciences, 9, 114

Cegla H. M., Shelyag S., Watson C. A., Mathioudakis M., 2013, ApJ, 763, L95

Cegla H. M. et al., 2018, ApJ, 866, L55

Cegla H. M., Watson C. A., Shelyag S., Mathioudakis M., Moutari S., 2019, ApJ, 879, L55

Chaplin W. J., Cegla H. M., Watson C. A., Davies G. R., Ball W. H., 2019, AJ, 157, 163

Collier Cameron A. et al., 2021, MNRAS, 505, 1699

Cosentino R. et al., 2012, in McLean I. S., Ramsay S. K., Takami H., eds, Proc. SPIE Conf. Ser.Vol. 8446, Ground-based and Airborne Instrumentation for Astronomy IV. SPIE, Bellingham, p. 84461V

Cranmer S. R., Saar S. H., 2011, ApJ, 741, L54

Cretignier M., Dumusque X., Hara N. C., Pepe F., 2021, A&A, 653, 43

Cretignier M., Dumusque X., Pepe F., 2022, A&A, 659, 68

Crétignier M., Pietrow A. G. M., Aigrain S., 2024, MNRAS, 527, 2940

Cui X.-Q. et al., 2012, RAA, 12, 1197

Curtis J. L. et al., 2020, ApJ, 904, L140

David T. J., Angus R., Curtis J. L., van Saders J. L., Colman I. L., Contardo G., Lu Y., Zinn J. C., 2022, ApJ, 933, L114

Davis A. B., Cisewski J., Dumusque X., Fischer D. A., Ford E. B., 2017, ApJ, 846, L59

Delisle J. B., Unger N., Hara N. C., Ségransan D., 2022, A&A, 659, 182

Donati J. F. et al., 2014, MNRAS, 444, 3220

Douglas S. T., Curtis J. L., Agüeros M. A., Cargile P. A., Brewer J. M., Meibom S., Jansen T., 2019, ApJ, 879, L100

Dumusque X., Udry S., Lovis C., Santos N. C., Monteiro M. J. P. F. G., 2011a, A&A, 525, 140

Dumusque X. et al., 2011b, A&A, 535, 55

Dumusque X., Boisse I., Santos N. C., 2014, ApJ, 796, L132

Faria J. P. et al., 2022, A&A, 658, 115

Foing B. H., 1988, Irish Astronomical Journal, 18, 257

Gaia Collaboration, 2016, A&A, 595, 1

Gaia Collaboration, 2018, A&A, 616, 1

Gibson S. R., Howard A. W., Marcy G. W., Edelstein J., Wishnow E. H., Poppett C. L., 2016, in Evans C. J., Simard L., Takami H., eds, Proc. SPIE Conf. Ser.Vol. 9908, Ground-based and Airborne Instrumentation for Astronomy VI. SPIE, Bellingham, p. 990870

Ginsburg A. et al., 2019, AJ, 157, 98

Gomes da Silva J., Figueira P., Santos N., Faria J., 2018, The J. Open Source Softw., 3, 667

Gomes da Silva J. et al., 2021, A&A, 646, 77

Gordon T. A., Davenport J. R. A., Angus R., Foreman-Mackey D., Agol E., Covey K. R., Agüeros M. A., Kipping D., 2021, ApJ, 913, L70

Hall O. J. et al., 2021, Nature Astron., 5, 707

Handley W. J., Hobson M. P., Lasenby A. N., 2015a, MNRAS, 450, 61

Handley W. J., Hobson M. P., Lasenby A. N., 2015b, MNRAS, 453, 4384

Hara N. C., Boué G., Laskar J., Correia A. C. M., 2017, MNRAS, 464, 1220

Haywood R. D. et al., 2022, ApJ, 935, L6

Isaacson H., Fischer D., 2010, ApJ, 725, L875

John A. A., Collier Cameron A., Wilson T. G., 2022, MNRAS, 515, 3975

Johnstone C. P., Bartel M., Güdel M., 2021, A&A, 649, 96

Jones D. E., Stenning D. C., Ford E. B., Wolpert R. L., Loredo T. J., Gilbertson C., Dumusque X., 2017, preprint (arXiv:1711.01318)

Jurgenson C., Fischer D., McCracken T., Sawyer D., Szymkowiak A., Davis A., Muller G., Santoro F., 2016, in Evans C. J., Simard L., Takami H., eds, Proc. SPIE Conf. Ser.Vol. 9908, Ground-based and Airborne Instrumentation for Astronomy VI. SPIE, Bellingham, p. 2051

Kjeldsen H., Bedding T. R., 1995, A&A, 293, 87

Lanzafame A. C., Spada F., 2015, A&A, 584, 30

Mayor M., Queloz D., 1995, Nature, 378, 355

Mayor M. et al., 2003, The Messenger, 114, 20

McQuillan A., Aigrain S., Mazeh T., 2013, MNRAS, 432, 1203

McQuillan A., Mazeh T., Aigrain S., 2014, ApJS, 211, 24

Meibom S., Mathieu R. D., Stassun K. G., 2009, ApJ, 695, L679

Meunier N., Lagrange A. M., 2019, A&A, 625, 6

Meunier N., Desort M., Lagrange A. M., 2010, A&A, 512, 39

Meunier N., Lagrange A. M., Borgniet S., Rieutord M., 2015, A&A, 583, 118

Meunier N., Lagrange A. M., Cuzacq S., 2019, A&A, 632, 81

Mortier A., Collier Cameron A., 2017, A&A, 601, 110

Nicholson B. A., Aigrain S., 2022, MNRAS, 515, 5251

Noyes R. W., Hartmann L. W., Baliunas S. L., Duncan D. K., Vaughan A. H., 1984, ApJ, 279, L763

Pepe F. et al., 2021, A&A, 645, 96

Prša A. et al., 2016, AJ, 152, 41

Rajpaul V., Aigrain S., Osborne M. A., Reece S., Roberts S., 2015, MNRAS, 452, 2269

Rajpaul V., Aigrain S., Roberts S., 2016, MNRAS, 456, 6

Rasmussen C. E., Williams C. K. I., 2006, Gaussian Processes for Machine Learning. MIT Press, Cambridge, MA

Reiners A., Schüssler M., Passegger V. M., 2014, ApJ, 794, L144

Reiners A. et al., 2022, A&A, 662, 41

Réville V., Brun A. S., Strugarek A., Matt S. P., Bouvier J., Folsom C. P., Petit P., 2015, ApJ, 814, L99

Roberts S., Osborne M., Ebden M., Reece S., Gibson N., Aigrain S., 2017, Phil. Trans. R. Soc. A: Math. Phys. Eng. Sci., 371, 20110550
Schwab C. et al., 2018, in Evans C. J., Simard L., Takami H., eds, Proc. SPIE Conf. Ser.Vol. 10702, Ground-based and Airborne Instrumentation for Astronomy VII. SPIE, Bellingham, p. 1070271
Skumanich A., 1972, ApJ, 171, L565
Snodgrass H. B., Ulrich R. K., 1990, ApJ, 351, L309
Spada F., Lanzafame A. C., 2020, A&A, 636, 76
Spada F., Lanzafame A. C., Lanza A. F., Messina S., Collier Cameron A., 2011, MNRAS, 416, 447
Strassmeier K. G., Ilyin I., Steffen M., 2018, A&A, 612, 44
Suárez Mascareño A. et al., 2020, A&A, 639, 77
Thompson S. J. et al., 2016, in Evans C. J., Simard L., Takami H., eds, Proc. SPIE Conf. Ser.Vol. 9908, Ground-based and Airborne Instrumentation for Astronomy VI. SPIE, Bellingham, p. 1949
Thompson A. P. G., Watson C. A., de Mooij E. J. W., Jess D. B., 2017, MNRAS, 468, 16
van Saders J. L., Ceillier T., Metcalfe T. S., Silva Aguirre V., Pinsonneault M. H., García R. A., Mathur S., Davies G. R., 2016, Nature, 529, 181
van Saders J. L., Pinsonneault M. H., Barbieri M., 2019, ApJ, 872, L128
Vidotto A. A. et al., 2014, MNRAS, 441, 2361
Wenger M. et al., 2000, A&AS, 143, 9
Zhao G., Zhao Y.-H., Chu Y.-Q., Jing Y.-P., Deng L.-C., 2012, RAA, 12, 723
Zhao L. L. et al., 2022a, AJ, 163, 171
Zhao J., Ford E. B., Tinney C. G., 2022b, ApJ, 935, L75

APPENDIX A: CONFIRMED ROTATION PERIOD MEASUREMENTS

Table A1 shows the measured rotation periods P_{rot} for the selected 49 targets. In addition to P_{rot}, we have provided information about the time span of the data T_{span}, as well as all other hyperparameters from our model, including the evolution time-scale l and the harmonic complexity Γ. We have also included the derived Rossby number Ro and the RMS[$aG(t)$] RMS[$b\dot{G}(t)$] (A/B; representing the facular-to-spot ratio). All values, except for T_{span}, come with associated uncertainties.

Table A1. Confirmed rotation period measurements of 49 targets.

Simbad name	T_{span} [yr]	P_{rot} [d]	l [d]	Γ	Ro	A/B
BD-08 2823	2.42	$27.0^{+0.4}_{-0.4}$	966^{+559}_{-462}	$1.86^{+0.91}_{-0.64}$	$0.94^{+0.02}_{-0.02}$	$1.5^{+1.0}_{-1.0}$
HD 104067	2.38	$30.3^{+0.8}_{-0.8}$	386^{+379}_{-230}	$1.21^{+0.66}_{-0.51}$	$1.25^{+0.03}_{-0.03}$	$0.7^{+0.6}_{-0.6}$
HD 109200	7.24	$39.6^{+8.3}_{-8.3}$	57^{+32}_{-38}	$0.76^{+0.34}_{-0.12}$	$1.72^{+0.36}_{-0.36}$	$1.8^{+0.5}_{-0.5}$
HD 115617	7.49	$32.1^{+0.2}_{-0.2}$	186^{+78}_{-50}	$0.68^{+0.16}_{-0.12}$	$1.99^{+0.02}_{-0.02}$	$1.2^{+0.7}_{-0.7}$
HD 125072	7.44	$40.8^{+0.8}_{-0.8}$	482^{+455}_{-227}	$1.14^{+0.47}_{-0.32}$	$1.52^{+0.03}_{-0.03}$	$1.9^{+1.5}_{-1.5}$
HD 125184	9.38	$43.9^{+2.0}_{-2.0}$	200^{+151}_{-78}	$0.59^{+0.19}_{-0.14}$	$3.06^{+0.14}_{-0.14}$	$1.8^{+1.2}_{-1.2}$
HD 125595	3.44	$37.1^{+0.5}_{-0.5}$	804^{+485}_{-410}	$2.82^{+1.78}_{-1.33}$	$1.27^{+0.02}_{-0.02}$	$1.2^{+1.0}_{-1.0}$
HD 13060	0.39	$34.3^{+3.8}_{-3.8}$	538^{+420}_{-272}	$3.91^{+3.06}_{-1.75}$	$1.68^{+0.19}_{-0.19}$	$0.8^{+0.7}_{-0.7}$
HD 136713	9.49	$36.4^{+1.6}_{-1.6}$	395^{+527}_{-231}	$0.87^{+0.48}_{-0.35}$	$1.52^{+0.07}_{-0.07}$	$0.3^{+0.3}_{-0.3}$
HD 13808	8.08	$38.0^{+0.3}_{-0.3}$	379^{+197}_{-106}	$1.20^{+0.28}_{-0.20}$	$1.62^{+0.01}_{-0.01}$	$3.1^{+2.0}_{-2.0}$
HD 144628	9.44	$38.5^{+1.1}_{-1.1}$	184^{+135}_{-64}	$1.59^{+0.64}_{-0.38}$	$1.63^{+0.05}_{-0.05}$	$3.5^{+2.7}_{-2.7}$
HD 15337	10.94	$37.1^{+0.8}_{-0.8}$	1330^{+456}_{-513}	$5.43^{+2.72}_{-2.48}$	$1.73^{+0.04}_{-0.04}$	$3.0^{+2.5}_{-2.5}$
HD 154088	5.25	$30.7^{+1.7}_{-1.7}$	150^{+66}_{-38}	$1.53^{+0.54}_{-0.35}$	$1.64^{+0.09}_{-0.09}$	$14.7^{+12.8}_{-12.8}$
HD 154577	7.44	$34.3^{+1.0}_{-1.0}$	104^{+42}_{-30}	$1.00^{+0.17}_{-0.14}$	$1.32^{+0.04}_{-0.04}$	$1.7^{+0.5}_{-0.5}$
HD 157172	5.40	$35.4^{+10.6}_{-10.6}$	498^{+478}_{-247}	$4.23^{+2.96}_{-2.16}$	$2.00^{+0.60}_{-0.60}$	$4.7^{+3.4}_{-3.4}$
HD 157830	2.56	$25.4^{+5.4}_{-5.4}$	566^{+722}_{-332}	$3.46^{+2.45}_{-1.48}$	$1.55^{+0.33}_{-0.33}$	$0.8^{+0.4}_{-0.4}$
HD 161098	9.43	$27.5^{+0.2}_{-0.2}$	323^{+163}_{-94}	$1.00^{+0.37}_{-0.22}$	$1.71^{+0.01}_{-0.01}$	$1.6^{+1.2}_{-1.2}$
HD 16417	3.33	$33.0^{+6.1}_{-6.1}$	102^{+90}_{-38}	$0.83^{+0.51}_{-0.23}$	$2.81^{+0.52}_{-0.52}$	$1.3^{+1.4}_{-1.4}$
HD 168863	2.36	$32.0^{+7.8}_{-7.8}$	1000^{+605}_{-529}	$2.58^{+2.71}_{-1.28}$	$1.19^{+0.29}_{-0.29}$	$2.0^{+2.5}_{-2.5}$
HD 171587	2.56	$24.7^{+3.3}_{-3.3}$	650^{+583}_{-390}	$2.76^{+1.95}_{-1.18}$	$1.35^{+0.18}_{-0.18}$	$1.3^{+0.9}_{-0.9}$
HD 172513	1.18	$24.0^{+0.6}_{-0.6}$	276^{+173}_{-127}	$1.14^{+0.40}_{-0.34}$	$1.41^{+0.03}_{-0.03}$	$1.0^{+0.6}_{-0.6}$
HD 176986	10.06	$34.8^{+0.8}_{-0.8}$	95^{+34}_{-24}	$0.65^{+0.12}_{-0.11}$	$1.48^{+0.03}_{-0.03}$	$1.1^{+0.4}_{-0.4}$
HD 183658	3.40	$28.4^{+8.2}_{-8.2}$	803^{+535}_{-460}	$3.57^{+2.85}_{-2.03}$	$2.300^{+0.66}_{-0.66}$	–
HD 189567	9.04	$41.7^{+11.7}_{-11.7}$	75^{+52}_{-62}	$0.64^{+0.89}_{-0.11}$	$3.06^{+0.86}_{-0.86}$	$6.5^{+2.3}_{-2.3}$
HD 192310	7.23	$41.0^{+0.9}_{-0.9}$	222^{+175}_{-64}	$1.23^{+0.37}_{-0.21}$	$1.81^{+0.04}_{-0.04}$	$2.5^{+2.8}_{-2.8}$
HD 202206	1.29	$50.0^{+5.1}_{-5.1}$	918^{+406}_{-352}	$5.54^{+2.27}_{-2.04}$	$3.810^{+0.39}_{-0.39}$	–
HD 208704	2.28	$32.2^{+7.8}_{-7.8}$	878^{+615}_{-507}	$3.10^{+2.29}_{-1.47}$	$2.69^{+0.65}_{-0.65}$	$2.0^{+2.1}_{-2.1}$
HD 215152	8.10	$38.0^{+0.8}_{-0.8}$	182^{+70}_{-42}	$2.59^{+0.86}_{-0.59}$	$1.43^{+0.03}_{-0.03}$	$4.7^{+3.1}_{-3.1}$
HD 216770	9.26	$37.4^{+4.7}_{-4.7}$	314^{+221}_{-149}	$1.57^{+0.81}_{-0.51}$	$2.07^{+0.26}_{-0.26}$	$1.0^{+1.0}_{-1.0}$
HD 21693	5.47	$32.0^{+0.7}_{-0.7}$	321^{+294}_{-119}	$0.84^{+0.31}_{-0.17}$	$1.78^{+0.04}_{-0.04}$	$3.4^{+2.8}_{-2.8}$
HD 21749	0.39	$38.3^{+4.9}_{-4.9}$	382^{+353}_{-222}	$1.45^{+0.60}_{-0.47}$	$1.32^{+0.17}_{-0.17}$	$0.4^{+0.3}_{-0.3}$
HD 22049	0.23	$11.2^{+0.1}_{-0.1}$	128^{+74}_{-56}	$1.70^{+0.58}_{-0.58}$	$0.48^{+0.01}_{-0.01}$	$0.1^{+0.1}_{-0.1}$
HD 223171	12.48	$37.2^{+11.2}_{-11.2}$	85^{+163}_{-64}	$0.98^{+2.82}_{-0.38}$	$3.170^{+0.95}_{-0.95}$	–
HD 26965	12.41	$35.6^{+16.0}_{-16.0}$	51^{+52}_{-40}	$1.64^{+3.74}_{-0.77}$	$1.560^{+0.70}_{-0.70}$	–

Table A1 – *continued*

Simbad name	T_{span} [yr]	P_{rot} [d]	l [d]	Γ	Ro	A/B
HD 27894	13.56	$48.2^{+8.0}_{-8.0}$	827^{+762}_{-635}	$3.34^{+2.80}_{-1.60}$	$1.968^{+0.32}_{-0.32}$	–
HD 36003	11.21	$50.2^{+2.0}_{-2.0}$	214^{+129}_{-78}	$0.85^{+0.22}_{-0.15}$	$1.74^{+0.07}_{-0.07}$	$2.4^{+1.3}_{-1.3}$
HD 40307	7.42	$42.5^{+0.5}_{-0.5}$	494^{+273}_{-139}	$1.21^{+0.29}_{-0.20}$	$1.76^{+0.02}_{-0.02}$	$2.5^{+1.6}_{-1.6}$
HD 45184	15.01	$20.0^{+0.1}_{-0.1}$	278^{+115}_{-78}	$1.22^{+0.27}_{-0.21}$	$1.78^{+0.01}_{-0.01}$	$5.6^{+3.0}_{-3.0}$
HD 4915	13.33	$25.2^{+11.7}_{-11.7}$	180^{+326}_{-163}	$2.49^{+2.46}_{-1.28}$	$1.72^{+0.80}_{-0.80}$	$2.3^{+1.9}_{-1.9}$
HD 51608	7.43	$37.1^{+1.8}_{-1.8}$	845^{+762}_{-527}	$1.60^{+1.10}_{-0.52}$	$1.95^{+0.10}_{-0.10}$	$3.1^{+2.8}_{-2.8}$
HD 63765	12.33	$25.5^{+9.1}_{-9.1}$	95^{+82}_{-42}	$3.20^{+3.15}_{-1.59}$	$1.42^{+0.51}_{-0.51}$	$1.6^{+1.5}_{-1.5}$
HD 65277A	2.43	$42.9^{+5.8}_{-5.8}$	1368^{+426}_{-501}	$5.28^{+2.56}_{-2.04}$	$1.52^{+0.20}_{-0.20}$	$0.7^{+0.9}_{-0.9}$
HD 68978	8.24	$16.8^{+0.8}_{-0.8}$	63^{+30}_{-20}	$0.73^{+0.20}_{-0.13}$	$1.75^{+0.08}_{-0.08}$	$2.2^{+1.1}_{-1.1}$
HD 69830	7.50	$33.7^{+1.0}_{-1.0}$	234^{+418}_{-106}	$1.31^{+0.63}_{-0.31}$	$1.83^{+0.06}_{-0.06}$	$2.5^{+1.8}_{-1.8}$
HD 71835	7.47	$29.7^{+0.5}_{-0.5}$	1123^{+583}_{-595}	$2.06^{+1.80}_{-0.70}$	$1.66^{+0.03}_{-0.03}$	$5.0^{+4.2}_{-4.2}$
HD 78429	13.37	$43.4^{+14.8}_{-14.8}$	19^{+58}_{-8}	$0.84^{+5.90}_{-0.33}$	$3.32^{+1.13}_{-1.13}$	$4.4^{+1.5}_{-1.5}$
HD 89454	1.43	$16.4^{+1.9}_{-1.9}$	327^{+278}_{-187}	$1.07^{+0.47}_{-0.36}$	$1.21^{+0.14}_{-0.14}$	$0.6^{+0.5}_{-0.5}$
HD 93083	10.26	$44.6^{+6.2}_{-6.2}$	321^{+448}_{-213}	$1.75^{+1.06}_{-0.66}$	$1.92^{+0.27}_{-0.27}$	$2.1^{+1.9}_{-1.9}$
HD 96700	5.33	$43.6^{+2.3}_{-2.3}$	194^{+177}_{-72}	$0.79^{+0.46}_{-0.21}$	$3.73^{+0.20}_{-0.20}$	$6.3^{+11.6}_{-11.6}$

APPENDIX B: BASIC PROPERTIES OF THE SAMPLE

Table B1 shows the basic properties of all 268 targets in the sample, including the effective temperature $T_{\rm eff}$, surface gravity log g, and mean log $R'_{\rm HK}$ from the catalogue provided by Gomes da Silva et al. (2021), with associated uncertainties. Additionally, we have included details about the temporal coverage of observations, denoted as $T_{\rm range}$, as well as the temporal span of the data processed using DRS 3.5. Any temporal span not covered by the DRS 3.5 processed data is filled by the DRS 3.8 processed data.

Table B1. Basic properties of all 268 targets in the sample.

Simbad name	$T_{\rm eff}$ [K]	$T_{\rm eff}$ err [K]	log g	log g err	Mean log $R'_{\rm HK}$	Mean log $R'_{\rm HK}$ err	$T_{\rm range}$	$T_{\rm range}$ (DRS 3.5)
BD-08 2823	4672.0	105.0	4.61	0.26	–4.6944	0.0039	2004–01 to 2018–04	2004–01 to 2010–01
CD-23 395	4673.0	175.0	4.52	0.47	–4.8528	0.0040	2004–07 to 2016–10	2004–07 to 2013–01
CD-24 10619	4574.0	155.0	4.68	0.44	–4.5766	0.0036	2005–06 to 2021–02	2005–06 to 2011–07
CD-26 2288	4924.0	94.0	4.51	0.28	–4.6539	0.0037	2004–01 to 2019–10	2004–01 to 2011–12
HD 10180	5911.0	19.0	4.19	0.03	–4.9957	0.0043	2003–11 to 2017–08	2003–11 to 2015–01
HD 101930	5164.0	61.0	4.49	0.11	–5.0048	0.0033	2004–02 to 2016–06	2004–02 to 2015–05
HD 102117	5657.0	24.0	4.21	0.04	–5.1215	0.0050	2004–01 to 2016–05	2004–01 to 2015–05
HD 102365	5629.0	29.0	4.35	0.03	–4.9489	0.0030	2003–11 to 2017–05	2003–11 to 2015–05
HD 103197	5250.0	60.0	4.51	0.11	–5.0796	0.0059	2004–02 to 2018–04	2004–02 to 2010–04
HD 103720	5017.0	88.0	4.58	0.16	–4.4493	0.0038	2005–02 to 2021–02	2005–02 to 2015–05
HD 103774	6732.0	56.0	4.29	0.06	–4.7718	0.0073	2004–12 to 2018–04	2004–12 to 2013–02
HD 104067	4969.0	72.0	4.64	0.13	–4.7370	0.0017	2004–02 to 2010–04	2004–02 to 2010–04
HD 104800	5697.0	25.0	4.35	0.02	–4.8877	0.0058	2004–02 to 2015–01	2004–02 to 2015–01
HD 105690	5666.0	38.0	4.53	0.07	–4.3063	0.0012	2009–04 to 2017–06	2009–04 to 2014–07
HD 106116	5680.0	15.0	4.28	0.03	–5.0317	0.0041	2004–02 to 2017–06	2004–02 to 2015–05
HD 10647	6218.0	20.0	4.30	0.04	–4.7431	0.0024	2003–11 to 2020–01	2003–11 to 2012–01
HD 10700	5310.0	17.0	4.49	0.03	–4.9773	0.0025	2003–09 to 2012–10	2003–10 to 2012–10
HD 107094	5562.0	17.0	4.48	0.03	–4.8283	0.0055	2004–01 to 2021–02	2004–01 to 2015–03
HD 109200	5056.0	33.0	4.50	0.08	–4.9542	0.0027	2004–02 to 2018–05	2004–02 to 2015–05
HD 109271	5783.0	18.0	4.13	0.02	–4.9963	0.0074	2005–02 to 2018–04	2005–02 to 2014–07
HD 111232	5460.0	21.0	4.41	0.03	–4.9832	0.0041	2004–02 to 2021–03	2004–02 to 2015–05
HD 111515	5398.0	18.0	4.47	0.02	–4.9528	0.0043	2004–02 to 2017–07	2004–02 to 2009–03
HD 111777	5666.0	19.0	4.36	0.03	–4.9115	0.0048	2004–02 to 2018–06	2004–02 to 2014–05
HD 11397	5564.0	26.0	4.40	0.04	–4.8975	0.0047	2003–10 to 2019–09	2003–10 to 2014–08
HD 114076	5066.0	25.1	4.47	0.07	–4.9911	0.0058	2004–02 to 2015–04	2004–02 to 2015–04
HD 114613	5729.0	17.0	3.84	0.02	–5.1529	0.0041	2004–01 to 2019–04	2004–01 to 2015–05
HD 114729	5844.0	12.0	4.02	0.02	–5.0046	0.0044	2004–02 to 2021–03	2004–02 to 2014–08
HD 114853	5705.0	14.0	4.32	0.02	–4.9435	0.0037	2004–01 to 2017–08	2004–01 to 2015–05
HD 115617	5559.0	17.0	4.30	0.03	–5.0132	0.0029	2004–01 to 2021–03	2004–01 to 2015–05
HD 117207	5667.0	21.0	4.22	0.04	–5.0881	0.0045	2004–02 to 2021–03	2004–02 to 2015–05
HD 117618	5990.0	13.0	4.18	0.02	–4.9790	0.0040	2004–02 to 2019–08	2004–02 to 2010–05
HD 119173	5779.0	44.0	4.11	0.04	–4.8290	0.0050	2006–02 to 2020–02	2006–02 to 2014–03

Table B1 – *continued*

Simbad name	$T_{\rm eff}$ [K]	$T_{\rm eff}$ err [K]	log g	log g err	Mean log $R'_{\rm HK}$	Mean log $R'_{\rm HK}$ err	T$_{\rm range}$	T$_{\rm range}$ (DRS 3.5)
HD 11964	5326.0	19.0	3.90	0.04	−5.1763	0.0037	2003–10 to 2018–11	2003–10 to 2015–01
HD 119949	6359.0	36.0	4.10	0.04	−4.9050	0.0046	2004–02 to 2014–01	2004–02 to 2014–01
HD 124292	5443.0	22.0	4.35	0.04	−5.0128	0.0037	2004–02 to 2017–08	2004–02 to 2015–05
HD 125072	4794.0	102.0	4.51	0.24	−4.9238	0.0018	2004–02 to 2017–08	2004–02 to 2015–05
HD 125184	5680.0	30.0	3.99	0.05	−5.0952	0.0039	2004–02 to 2017–08	2004–02 to 2015–05
HD 125595	4636.0	83.9	4.50	0.26	−4.7575	0.0030	2004–05 to 2019–08	2004–05 to 2010–02
HD 125612A	5913.0	17.0	4.23	0.03	−4.8988	0.0083	2004–02 to 2021–03	2004–02 to 2015–03
HD 125881	6036.0	17.0	4.24	0.03	−4.8726	0.0036	2004–02 to 2013–05	2004–02 to 2013–05
HD 126525	5638.0	13.0	4.28	0.02	−4.9978	0.0045	2004–06 to 2019–05	2004–06 to 2015–05
HD 126793	5904.0	33.0	4.23	0.03	−4.8659	0.0048	2004–05 to 2015–02	2004–05 to 2015–02
HD 126803	5470.0	18.0	4.45	0.04	−4.9348	0.0050	2004–02 to 2019–08	2004–02 to 2014–05
HD 129642	4919.0	65.0	4.54	0.16	−5.0077	0.0037	2004–02 to 2017–08	2004–02 to 2015–05
HD 13060	5255.0	45.0	4.40	0.09	−4.8547	0.0051	2003–10 to 2016–09	2003–10 to 2015–01
HD 131653	5324.0	26.0	4.57	0.04	−4.9976	0.0077	2004–05 to 2015–07	2004–05 to 2015–05
HD 131664	5901.0	26.0	4.30	0.03	−4.8432	0.0076	2004–05 to 2021–02	2004–05 to 2014–07
HD 132569	4967.0	44.7	4.64	0.11	−4.6443	0.0043	2004–05 to 2011–08	2004–05 to 2011–08
HD 133633	5571.0	19.0	4.41	0.04	−4.9437	0.0053	2005–05 to 2018–07	2005–05 to 2014–05
HD 134060	5966.0	14.0	4.21	0.03	−4.9983	0.0038	2004–02 to 2017–05	2004–02 to 2015–05
HD 134088	5675.0	22.0	4.35	0.03	−4.8092	0.0041	2004–05 to 2015–06	2004–05 to 2015–04
HD 134606	5633.0	28.0	4.29	0.05	−5.1077	0.0042	2004–07 to 2017–05	2004–07 to 2015–05
HD 134987	5740.0	23.0	4.17	0.04	−5.1106	0.0043	2004–02 to 2016–04	2004–02 to 2015–05
HD 135625	6003.0	14.0	4.08	0.04	−5.0250	0.0087	2004–02 to 2021–03	2004–02 to 2015–05
HD 136352	5664.0	14.0	4.29	0.02	−4.9412	0.0031	2004–05 to 2017–08	2004–05 to 2015–05
HD 136713	4994.0	74.0	4.61	0.14	−4.7748	0.0020	2005–05 to 2016–09	2005–05 to 2015–05
HD 137388	5240.0	53.0	4.48	0.11	−4.8949	0.0040	2005–07 to 2016–08	2005–07 to 2014–06
HD 137676	5253.0	18.0	3.99	0.03	−5.1132	0.0044	2004–02 to 2018–06	2004–02 to 2011–08
HD 13808	5033.0	38.0	4.50	0.08	−4.8921	0.0034	2003–12 to 2016–02	2003–12 to 2015–01
HD 1388	5954.0	10.0	4.19	0.02	−4.9714	0.0038	2003–10 to 2017–09	2003–10 to 2014–12
HD 141624	5871.0	30.0	4.22	0.03	−4.9127	0.0050	2005–05 to 2018–08	2005–05 to 2014–07
HD 142709	4728.0	65.0	4.70	0.18	−4.9360	0.0023	2004–07 to 2016–04	2004–07 to 2015–02
HD 143361	5503.0	36.0	4.32	0.06	−5.1130	0.0072	2007–05 to 2020–03	2007–05 to 2014–09
HD 144628	5022.0	26.0	4.58	0.08	−4.9259	0.0025	2004–07 to 2019–04	2004–07 to 2015–05
HD 145377	6054.0	16.0	4.27	0.03	−4.6128	0.0051	2005–06 to 2011–04	2005–06 to 2011–04
HD 145417	4953.0	48.4	4.98	0.08	−4.8971	0.0032	2004–05 to 2014–08	2004–05 to 2014–08
HD 14745	6290.0	39.0	4.37	0.04	−4.8876	0.0073	2003–11 to 2021–02	2003–11 to 2014–03
HD 148156	6251.0	25.0	4.18	0.05	−4.9315	0.0087	2005–04 to 2019–07	2005–04 to 2013–07
HD 148211	5948.0	22.0	4.15	0.02	−4.9037	0.0050	2004–05 to 2016–04	2004–05 to 2015–03
HD 148303	4829.0	84.0	4.66	0.22	−4.6532	0.0022	2004–07 to 2013–05	2004–07 to 2013–05
HD 149396	5657.0	23.0	4.37	0.03	−4.6836	0.0056	2004–09 to 2016–05	2004–09 to 2013–07
HD 150177	6216.0	28.0	3.86	0.03	−4.8915	0.0041	2004–05 to 2013–07	2004–05 to 2013–07
HD 150433	5665.0	12.0	4.33	0.02	−4.9512	0.0038	2005–08 to 2017–08	2005–08 to 2014–09
HD 15337	5179.0	44.0	4.48	0.09	−4.9226	0.0039	2003–12 to 2019–09	2003–12 to 2015–01
HD 153950	6074.0	15.0	4.13	0.03	−4.9721	0.0082	2005–05 to 2018–03	2005–05 to 2014–07
HD 154088	5374.0	43.0	4.38	0.07	−5.0718	0.0029	2006–04 to 2017–08	2006–04 to 2015–05
HD 154577	4847.0	35.0	4.69	0.07	−4.8699	0.0022	2004–05 to 2017–08	2004–05 to 2015–05
HD 156098	6517.0	44.0	3.76	0.05	−4.7816	0.0045	2005–05 to 2021–03	2005–05 to 2015–05
HD 15612	5256.0	34.0	4.55	0.06	−4.5080	0.0044	2003–11 to 2018–02	2003–11 to 2014–03
HD 156411	5910.0	16.0	3.79	0.01	−5.1400	0.0096	2005–05 to 2019–07	2005–05 to 2013–07
HD 157172	5451.0	27.0	4.37	0.05	−5.0040	0.0037	2005–07 to 2017–03	2005–07 to 2015–05
HD 157347	5676.0	16.0	4.27	0.03	−5.0213	0.0038	2006–03 to 2019–08	2006–03 to 2015–05
HD 157830	5540.0	16.0	4.43	0.02	−4.7868	0.0030	2004–05 to 2012–09	2004–05 to 2012–09
HD 1581	5951.0	13.0	4.28	0.03	−4.9174	0.0031	2003–10 to 2020–12	2003–10 to 2014–12
HD 16008	5770.0	14.0	4.33	0.03	−4.8465	0.0049	2003–10 to 2021–03	2003–10 to 2015–01
HD 161098	5560.0	15.0	4.40	0.02	−4.9240	0.0037	2006–04 to 2017–09	2006–04 to 2015–05
HD 161566	6230.0	24.0	3.88	0.04	−4.9879	0.0077	2005–06 to 2019–07	2005–06 to 2013–03
HD 16160	4796.0	109.0	4.62	0.27	−4.8649	0.0020	2003–10 to 2008–09	2003–10 to 2008–09
HD 16280	4677.0	83.5	4.58	0.31	−4.6712	0.0039	2003–10 to 2021–03	2003–10 to 2014–12
HD 16417	5841.0	17.0	3.99	0.02	−5.1028	0.0043	2003–11 to 2017–09	2003–11 to 2015–01
HD 165131	5870.0	15.0	4.27	0.03	−4.9658	0.0086	2006–05 to 2021–03	2006–05 to 2015–05
HD 166724	5099.0	36.0	4.55	0.09	−4.7253	0.0033	2004–05 to 2011–09	2004–05 to 2011–09
HD 167677	5474.0	20.0	4.40	0.03	−4.9899	0.0074	2005–05 to 2019–08	2005–05 to 2015–05
HD 168863	4782.0	80.0	4.52	0.23	−4.7762	0.0041	2006–07 to 2021–03	2006–07 to 2014–07
HD 170493	4751.0	108.0	4.49	0.25	−4.8776	0.0024	2005–07 to 2015–09	2005–07 to 2015–05
HD 171028	5671.0	16.0	3.73	0.03	−5.1098	0.0071	2004–10 to 2017–09	2004–10 to 2011–03

Table B1 – *continued*

Simbad name	T_{eff} [K]	T_{eff} err [K]	log g	log g err	Mean log R'_{HK}	Mean log R'_{HK} err	$\mathrm{T}_{\mathrm{range}}$	$\mathrm{T}_{\mathrm{range}}$ (DRS 3.5)
HD 171587	5412.0	15.0	4.58	0.02	–4.7553	0.0035	2004–11 to 2014–08	2004–11 to 2014–08
HD 172513	5500.0	18.0	4.37	0.03	–4.7730	0.0025	2004–05 to 2007–05	2004–05 to 2007–05
HD 172568	5728.0	22.0	4.45	0.03	–4.9046	0.0051	2005–05 to 2018–08	2005–05 to 2013–10
HD 175607	5392.0	17.0	4.51	0.03	–4.9298	0.0052	2004–07 to 2015–04	2004–07 to 2015–04
HD 176354	5271.0	40.0	3.89	0.07	–5.0505	0.0052	2006–05 to 2019–07	2006–05 to 2011–09
HD 176986	5018.0	59.0	4.60	0.11	–4.8283	0.0028	2004–07 to 2017–08	2004–07 to 2015–04
HD 177565	5627.0	19.0	4.30	0.03	–4.9085	0.0027	2003–10 to 2017–09	2003–10 to 2015–05
HD 17865	5877.0	24.0	4.13	0.03	–4.9272	0.0051	2003–11 to 2014–09	2003–11 to 2014–09
HD 17970	5038.0	31.0	4.53	0.06	–5.0043	0.0037	2003–10 to 2017–09	2003–10 to 2015–01
HD 181433	4962.0	134.0	4.54	0.27	–5.1290	0.0036	2003–10 to 2017–08	2003–10 to 2015–05
HD 181720	5792.0	17.0	4.10	0.02	–4.9792	0.0051	2005–05 to 2017–11	2005–05 to 2014–08
HD 183658	5803.0	17.0	4.24	0.02	–4.9407	0.0043	2005–08 to 2019–05	2005–08 to 2015–05
HD 185283	4746.0	79.3	4.53	0.20	–4.9514	0.0046	2005–07 to 2019–09	2005–07 to 2015–05
HD 189567	5726.0	15.0	4.28	0.01	–4.9120	0.0031	2003–10 to 2017–08	2003–10 to 2015–05
HD 190248	5644.0	30.0	4.12	0.05	–5.1315	0.0034	2003–10 to 2016–10	2003–10 to 2015–05
HD 190647	5639.0	24.0	4.09	0.04	–5.1613	0.0064	2004–09 to 2021–03	2004–09 to 2014–10
HD 190984	6007.0	25.0	3.78	0.03	–5.0626	0.0073	2004–05 to 2013–08	2004–05 to 2013–08
HD 191797	5037.0	48.5	4.61	0.11	–4.3751	0.0037	2004–07 to 2019–08	2004–07 to 2014–07
HD 192310	5087.0	48.0	4.42	0.10	–4.9509	0.0019	2003–11 to 2016–10	2003–11 to 2014–10
HD 19467	5720.0	10.0	4.18	0.01	–5.0079	0.0040	2003–10 to 2017–10	2003–10 to 2015–01
HD 195145	5625.0	20.0	4.32	0.03	–4.9820	0.0081	2006–07 to 2018–06	2006–07 to 2013–07
HD 19641	5806.0	14.0	4.23	0.02	–4.9734	0.0082	2003–11 to 2021–01	2003–11 to 2014–12
HD 197027	5694.0	28.0	4.09	0.04	–5.0001	0.0067	2009–05 to 2019–05	2009–05 to 2014–11
HD 197197	5812.0	16.0	4.04	0.02	–5.0203	0.0061	2003–11 to 2018–10	2003–11 to 2015–04
HD 199288	5765.0	19.0	4.36	0.02	–4.8868	0.0033	2003–11 to 2019–11	2003–11 to 2015–05
HD 199289	5928.0	37.0	4.43	0.03	–4.8466	0.0050	2003–11 to 2018–08	2003–11 to 2014–10
HD 199604	5817.0	22.0	4.18	0.03	–4.9118	0.0057	2003–11 to 2018–10	2003–11 to 2010–11
HD 199847	5763.0	20.0	4.08	0.02	–5.0033	0.0067	2003–11 to 2018–10	2003–11 to 2014–09
HD 20003	5494.0	27.0	4.37	0.05	–4.9891	0.0050	2003–12 to 2017–08	2003–12 to 2015–01
HD 200538	6042.0	18.0	4.13	0.03	–5.0017	0.0085	2004–09 to 2017–04	2004–09 to 2012–09
HD 202206	5757.0	25.0	4.33	0.03	–4.7434	0.0028	2004–05 to 2019–06	2004–05 to 2012–06
HD 202871	6055.0	16.0	4.28	0.04	–4.7825	0.0075	2005–06 to 2012–09	2005–06 to 2012–09
HD 20407	5866.0	14.0	4.32	0.01	–4.8786	0.0034	2003–10 to 2017–11	2003–10 to 2015–02
HD 204313	5776.0	22.0	4.23	0.02	–5.0384	0.0046	2006–05 to 2017–09	2006–05 to 2014–10
HD 204941	4997.0	36.0	4.52	0.10	–4.9275	0.0034	2004–12 to 2016–09	2004–12 to 2014–10
HD 205294	6370.0	32.0	3.92	0.04	–4.8884	0.0072	2003–10 to 2018–09	2003–10 to 2011–08
HD 205536	5442.0	23.0	4.36	0.04	–5.0377	0.0036	2003–10 to 2020–11	2003–10 to 2009–11
HD 206998	5822.0	26.0	4.08	0.03	–4.9271	0.0058	2003–11 to 2018–10	2003–11 to 2014–10
HD 2071	5719.0	14.0	4.35	0.02	–4.9186	0.0036	2003–10 to 2017–10	2003–10 to 2014–11
HD 207129	5937.0	13.0	4.28	0.02	–4.8853	0.0030	2003–10 to 2020–11	2003–10 to 2015–05
HD 20781	5256.0	29.0	4.43	0.05	–5.0498	0.0043	2003–12 to 2017–09	2003–12 to 2015–02
HD 20782	5774.0	14.0	4.22	0.01	–4.9044	0.0036	2003–10 to 2017–10	2003–10 to 2015–01
HD 207832	5718.0	27.0	4.33	0.04	–4.7324	0.0052	2003–10 to 2019–09	2003–10 to 2013–10
HD 207869	5527.0	21.0	4.45	0.05	–4.9486	0.0060	2003–11 to 2017–08	2003–11 to 2013–08
HD 20807	5824.0	15.0	4.29	0.03	–4.8720	0.0029	2003–10 to 2021–02	2003–10 to 2015–02
HD 208487	6146.0	19.0	4.19	0.03	–4.9230	0.0038	2004–09 to 2019–09	2004–09 to 2007–06
HD 20868	4720.0	91.0	4.50	0.22	–4.9930	0.0050	2003–11 to 2019–08	2003–11 to 2008–08
HD 208704	5826.0	11.0	4.21	0.01	–4.9438	0.0037	2004–07 to 2017–10	2004–07 to 2014–11
HD 210918	5755.0	12.0	4.21	0.02	–5.0101	0.0037	2003–10 to 2019–12	2003–10 to 2014–09
HD 211038	4974.0	17.0	3.84	0.05	–5.1615	0.0030	2003–11 to 2017–08	2003–11 to 2014–10
HD 21132	6243.0	34.0	4.27	0.05	–4.8531	0.0058	2004–02 to 2020–01	2004–02 to 2015–01
HD 21209	4671.0	65.0	4.59	0.15	–4.7945	0.0026	2003–10 to 2016–09	2003–10 to 2015–01
HD 215152	4803.0	52.0	4.49	0.15	–4.8599	0.0022	2003–12 to 2016–09	2003–12 to 2014–08
HD 215456	5789.0	15.0	3.95	0.03	–5.1311	0.0049	2003–10 to 2017–05	2003–10 to 2014–10
HD 215497	5003.0	103.0	4.41	0.26	–5.0695	0.0050	2004–10 to 2018–08	2004–10 to 2009–11
HD 216770	5424.0	51.0	4.37	0.07	–4.9645	0.0031	2003–10 to 2019–09	2003–10 to 2013–11
HD 21693	5430.0	26.0	4.36	0.04	–4.9244	0.0035	2003–10 to 2017–09	2003–10 to 2015–01
HD 21749	4640.0	100.0	4.91	0.07	–4.6899	0.0019	2003–11 to 2016–12	2003–11 to 2009–12
HD 218504	5962.0	29.0	4.12	0.03	–4.9327	0.0045	2003–11 to 2014–09	2003–11 to 2014–09
HD 219828	5888.0	14.0	4.01	0.02	–5.1190	0.0064	2005–05 to 2015–08	2005–05 to 2013–11
HD 220339	4938.0	32.0	4.60	0.08	–4.8213	0.0024	2003–10 to 2020–12	2003–10 to 2014–12
HD 22049	5049.0	48.0	4.59	0.09	–4.4937	0.0007	2003–11 to 2020–01	2003–11 to 2007–08
HD 220507	5698.0	17.0	4.17	0.03	–5.0747	0.0049	2003–10 to 2017–10	2003–10 to 2014–12
HD 221580	5322.0	24.0	2.71	0.04	–5.4860	0.0158	2003–11 to 2007–10	2003–11 to 2007–10

Table B1 – *continued*

Simbad name	$T_{\rm eff}$ [K]	$T_{\rm eff}$ err [K]	log g	log g err	Mean log $R'_{\rm HK}$	Mean log $R'_{\rm HK}$ err	$T_{\rm range}$	$T_{\rm range}$ (DRS 3.5)
HD 222669	5894.0	17.0	4.27	0.02	–4.8376	0.0038	2003–12 to 2016–10	2003–12 to 2014–12
HD 223171	5841.0	18.0	4.03	0.02	–5.0245	0.0042	2003–10 to 2018–11	2003–10 to 2014–12
HD 224685	5504.0	30.0	4.43	0.06	–4.9248	0.0064	2004–12 to 2018–08	2004–12 to 2014–12
HD 224817	5894.0	22.0	4.17	0.02	–4.9232	0.0052	2003–11 to 2015–07	2003–11 to 2014–11
HD 22879	5857.0	27.0	4.28	0.02	–4.8791	0.0035	2003–10 to 2017–10	2003–10 to 2015–01
HD 23249	5035.0	39.0	3.80	0.08	–5.1648	0.0024	2003–10 to 2017–03	2003–10 to 2015–01
HD 24062	6107.0	60.0	4.34	0.06	–5.0123	0.0086	2003–11 to 2021–03	2003–11 to 2013–11
HD 24633	5276.0	43.0	4.41	0.07	–4.9850	0.0071	2003–11 to 2021–03	2003–11 to 2013–12
HD 25171	6160.0	24.0	4.13	0.03	–4.9322	0.0068	2003–11 to 2020–12	2003–11 to 2015–02
HD 26965	5072.0	53.0	4.58	0.19	–4.9495	0.0022	2003–10 to 2021–02	2003–10 to 2015–01
HD 27063	5767.0	14.0	4.30	0.03	–4.7496	0.0029	2003–11 to 2008–02	2003–11 to 2008–02
HD 27894	4952.0	105.0	4.56	0.20	–4.9392	0.0065	2003–10 to 2019–03	2003–10 to 2013–11
HD 28254A	5653.0	33.0	4.05	0.05	–5.1685	0.0094	2003–10 to 2021–03	2003–10 to 2014–09
HD 28471	5745.0	14.0	4.24	0.01	–4.9963	0.0043	2003–11 to 2018–01	2003–11 to 2013–01
HD 297396	4622.0	114.0	4.58	0.36	–4.8059	0.0039	2004–01 to 2021–02	2004–01 to 2015–05
HD 31103	6078.0	16.0	4.23	0.02	–4.6294	0.0055	2003–11 to 2020–11	2003–11 to 2013–11
HD 31128	6096.0	67.0	4.63	0.06	–4.8146	0.0057	2003–11 to 2015–04	2003–11 to 2015–04
HD 31527	5898.0	13.0	4.26	0.02	–4.9395	0.0038	2003–10 to 2017–08	2003–10 to 2015–02
HD 31822	6042.0	16.0	4.32	0.03	–4.8204	0.0035	2003–10 to 2016–03	2003–10 to 2015–02
HD 3220	5846.0	15.0	4.34	0.02	–4.8183	0.0079	2003–11 to 2010–11	2003–11 to 2010–11
HD 32564	5533.0	29.0	4.31	0.06	–5.0305	0.0052	2009–11 to 2016–03	2009–11 to 2015–01
HD 330075	4958.0	52.0	4.41	0.13	–4.9777	0.0041	2004–02 to 2015–04	2004–02 to 2012–02
HD 35854	4928.0	56.0	4.64	0.11	–4.8052	0.0021	2003–10 to 2018–05	2003–10 to 2015–02
HD 36003	4647.0	88.0	4.60	0.21	–4.8609	0.0016	2003–12 to 2016–03	2003–12 to 2015–03
HD 36379	6030.0	14.0	4.05	0.02	–4.9482	0.0040	2003–10 to 2017–04	2003–10 to 2015–03
HD 3823	6022.0	14.0	4.07	0.02	–4.9692	0.0039	2003–10 to 2017–09	2003–10 to 2015–01
HD 38858	5733.0	12.0	4.38	0.01	–4.9051	0.0029	2003–10 to 2019–01	2003–10 to 2015–02
HD 39091	6003.0	17.0	4.18	0.03	–4.9815	0.0037	2003–12 to 2020–12	2003–12 to 2015–01
HD 39194	5205.0	23.0	4.61	0.05	–4.9628	0.0041	2003–11 to 2017–08	2003–11 to 2015–02
HD 3964	5729.0	19.0	4.37	0.04	–4.8328	0.0073	2003–11 to 2020–12	2003–11 to 2014–09
HD 40307	4977.0	59.0	4.63	0.16	–4.9389	0.0021	2003–10 to 2019–04	2003–10 to 2015–02
HD 40397	5527.0	20.0	4.34	0.04	–5.0316	0.0037	2003–10 to 2016–09	2003–10 to 2015–04
HD 40865	5719.0	16.0	4.38	0.03	–4.9144	0.0053	2003–10 to 2017–12	2003–10 to 2014–12
HD 41248	5713.0	21.0	4.37	0.03	–4.8806	0.0053	2003–10 to 2017–12	2003–10 to 2014–01
HD 4308	5644.0	16.0	4.28	0.03	–4.9553	0.0035	2003–10 to 2021–01	2003–10 to 2015–01
HD 43197	5449.0	42.0	4.28	0.08	–5.0857	0.0070	2003–12 to 2021–03	2003–12 to 2013–03
HD 44219	5766.0	18.0	4.06	0.03	–5.0551	0.0083	2003–11 to 2021–03	2003–11 to 2013–03
HD 45184	5869.0	14.0	4.29	0.02	–4.9011	0.0031	2003–10 to 2021–03	2003–10 to 2015–03
HD 45364	5434.0	20.0	4.37	0.03	–4.9753	0.0041	2003–12 to 2017–09	2003–12 to 2015–02
HD 457	6089.0	23.0	4.16	0.03	–5.0230	0.0085	2003–10 to 2020–11	2003–10 to 2014–12
HD 47186	5675.0	21.0	4.25	0.04	–5.0712	0.0043	2003–12 to 2017–09	2003–12 to 2015–04
HD 48115	5825.0	12.0	4.31	0.02	–4.7526	0.0070	2004–01 to 2020–11	2004–01 to 2011–01
HD 48265	5798.0	29.0	3.79	0.14	–5.1912	0.0063	2007–09 to 2021–03	2007–09 to 2015–02
HD 4915	5658.0	13.0	4.42	0.03	–4.7879	0.0025	2003–10 to 2020–12	2003–10 to 2008–09
HD 51608	5358.0	22.0	4.38	0.05	–5.0082	0.0043	2003–12 to 2017–09	2003–12 to 2015–04
HD 52265	6136.0	31.0	4.07	0.03	–4.9915	0.0043	2004–02 to 2021–02	2004–02 to 2010–04
HD 5388	6311.0	33.0	3.89	0.03	–4.9165	0.0082	2003–11 to 2019–07	2003–11 to 2010–01
HD 56274	5734.0	22.0	4.38	0.03	–4.8320	0.0034	2003–11 to 2015–04	2003–11 to 2015–04
HD 59468	5618.0	20.0	4.30	0.03	–5.0095	0.0034	2003–10 to 2018–05	2003–10 to 2015–05
HD 59711A	5722.0	13.0	4.33	0.02	–4.9295	0.0041	2003–10 to 2017–11	2003–10 to 2015–01
HD 60532	6273.0	37.0	3.68	0.04	–5.0976	0.0050	2006–02 to 2011–06	2006–02 to 2011–06
HD 61051	5363.0	27.0	4.38	0.05	–5.0692	0.0079	2004–01 to 2021–01	2004–01 to 2015–03
HD 61383	5716.0	14.0	4.08	0.02	–5.0179	0.0088	2003–12 to 2021–03	2003–12 to 2015–03
HD 61986	5725.0	20.0	4.35	0.04	–4.8898	0.0045	2003–12 to 2017–05	2003–12 to 2010–12
HD 63765	5432.0	19.0	4.41	0.03	–4.7358	0.0026	2003–12 to 2019–04	2003–12 to 2010–04
HD 65277A	4701.0	57.0	4.57	0.16	–5.0334	0.0025	2003–12 to 2017–01	2003–12 to 2015–05
HD 65907A	5945.0	16.0	4.31	0.02	–4.9009	0.0032	2003–10 to 2021–01	2003–10 to 2015–04
HD 68146	6427.0	44.0	4.12	0.04	–4.8606	0.0033	2006–02 to 2014–05	2006–02 to 2014–05
HD 68284	5933.0	26.0	3.87	0.03	–5.0952	0.0062	2003–11 to 2015–01	2003–11 to 2015–01
HD 68607	5215.0	45.0	4.48	0.08	–4.7254	0.0027	2003–12 to 2007–04	2003–12 to 2007–04
HD 68978	5965.0	22.0	4.26	0.02	–4.8548	0.0029	2003–10 to 2016–03	2003–10 to 2015–05
HD 69611	5762.0	25.0	4.17	0.03	–4.9562	0.0045	2003–11 to 2017–04	2003–11 to 2015–01
HD 69830	5402.0	28.0	4.40	0.04	–4.9989	0.0027	2003–10 to 2019–12	2003–10 to 2015–05
HD 70642	5668.0	22.0	4.30	0.04	–5.0217	0.0046	2003–12 to 2021–03	2003–12 to 2015–03

Table B1 – *continued*

Simbad name	T_{eff} [K]	T_{eff} err [K]	log g	log g err	Mean log R'_{HK}	Mean log R'_{HK} err	$\mathrm{T}_{\mathrm{range}}$	$\mathrm{T}_{\mathrm{range}}$ (DRS 3.5)
HD 71334	5694.0	13.0	4.26	0.03	–4.9853	0.0045	2003–12 to 2017–02	2003–12 to 2015–01
HD 71835	5438.0	22.0	4.37	0.04	–4.9417	0.0037	2003–12 to 2017–05	2003–12 to 2015–05
HD 7199	5386.0	45.0	4.34	0.08	–4.9891	0.0037	2003–11 to 2017–09	2003–11 to 2015–01
HD 72659	5926.0	12.0	4.03	0.01	–4.9963	0.0086	2004–02 to 2021–03	2004–02 to 2014–06
HD 72673	5243.0	22.0	4.52	0.04	–4.9259	0.0022	2003–12 to 2019–04	2003–12 to 2015–05
HD 73267	5373.0	30.0	4.38	0.05	–5.0939	0.0067	2004–01 to 2021–03	2004–01 to 2015–05
HD 73524	6017.0	13.0	4.19	0.03	–4.9962	0.0040	2003–12 to 2019–04	2003–12 to 2015–05
HD 73583	4597.0	69.0	4.57	0.28	–4.4603	0.0032	2004–02 to 2020–03	2004–02 to 2005–12
HD 7449	6024.0	13.0	4.27	0.03	–4.8206	0.0032	2003–11 to 2016–01	2003–11 to 2015–01
HD 74698	5783.0	19.0	4.12	0.02	–5.0331	0.0090	2004–02 to 2021–03	2004–02 to 2015–05
HD 74957	5915.0	20.0	4.34	0.03	–4.9276	0.0081	2004–01 to 2021–03	2004–01 to 2015–02
HD 76151	5788.0	23.0	4.33	0.02	–4.7266	0.0022	2003–11 to 2021–02	2003–11 to 2012–11
HD 77110	5717.0	20.0	4.36	0.02	–4.9256	0.0050	2004–01 to 2017–05	2004–01 to 2014–02
HD 77338	5440.0	52.0	4.34	0.11	–5.0587	0.0047	2004–12 to 2019–06	2004–12 to 2013–09
HD 78429	5760.0	19.0	4.19	0.02	–4.9518	0.0037	2003–12 to 2017–06	2003–12 to 2015–05
HD 79601	5825.0	25.0	4.15	0.03	–4.9291	0.0047	2004–01 to 2015–02	2004–01 to 2015–02
HD 82342	4470.0	21.0	4.96	0.05	–4.9746	0.0030	2003–12 to 2016–05	2003–12 to 2015–05
HD 82516	5041.0	57.0	4.61	0.12	–4.9816	0.0031	2003–12 to 2017–07	2003–12 to 2015–05
HD 82943	5989.0	20.0	4.20	0.02	–4.9623	0.0034	2004–01 to 2017–06	2004–01 to 2015–05
HD 8389A	5283.0	64.0	4.41	0.12	–5.0311	0.0028	2003–11 to 2020–12	2003–11 to 2013–09
HD 8535	6158.0	13.0	4.12	0.02	–4.9292	0.0081	2003–11 to 2019–08	2003–11 to 2014–10
HD 85390	5135.0	45.0	4.42	0.12	–4.9666	0.0037	2003–12 to 2017–05	2003–12 to 2015–05
HD 85725	5986.0	26.0	3.72	0.04	–5.2147	0.0093	2004–02 to 2021–02	2004–02 to 2015–05
HD 87838	6118.0	33.0	4.19	0.03	–4.8489	0.0045	2004–01 to 2017–07	2004–01 to 2015–05
HD 88218	5878.0	14.0	3.97	0.02	–5.0915	0.0045	2003–12 to 2016–05	2003–12 to 2015–05
HD 8828	5403.0	25.0	4.46	0.03	–5.0145	0.0042	2003–10 to 2017–09	2003–10 to 2015–01
HD 88725	5654.0	17.0	4.39	0.03	–4.8848	0.0039	2004–02 to 2015–06	2004–02 to 2014–12
HD 89454	5728.0	17.0	4.34	0.03	–4.6977	0.0024	2004–01 to 2008–01	2004–01 to 2008–01
HD 89839	6314.0	24.0	4.13	0.06	–4.9294	0.0080	2004–02 to 2021–02	2004–02 to 2015–05
HD 90156	5599.0	12.0	4.40	0.02	–4.9509	0.0034	2004–01 to 2017–07	2004–01 to 2015–05
HD 91889	6140.0	22.0	4.03	0.03	–4.8652	0.0031	2006–02 to 2011–02	2006–02 to 2011–02
HD 92719	5824.0	16.0	4.34	0.03	–4.8249	0.0027	2004–01 to 2016–05	2004–01 to 2015–04
HD 93083	5048.0	66.0	4.46	0.16	–4.9899	0.0031	2004–01 to 2017–07	2004–01 to 2015–04
HD 93385	5977.0	18.0	4.19	0.02	–4.9714	0.0043	2003–12 to 2017–05	2003–12 to 2015–04
HD 94151	5583.0	19.0	4.31	0.02	–4.9724	0.0038	2003–12 to 2019–04	2003–12 to 2013–03
HD 94771	5631.0	21.0	3.94	0.03	–5.2218	0.0090	2004–02 to 2021–03	2004–02 to 2015–05
HD 95456	6276.0	22.0	4.01	0.04	–4.9432	0.0038	2003–12 to 2017–06	2003–12 to 2015–05
HD 95542	5984.0	15.0	4.29	0.03	–4.6653	0.0068	2004–01 to 2020–12	2004–01 to 2015–03
HD 9578	6055.0	14.0	4.26	0.03	–4.5938	0.0055	2003–11 to 2020–11	2003–11 to 2012–11
HD 96423	5711.0	18.0	4.23	0.02	–5.0486	0.0042	2003–12 to 2019–05	2003–12 to 2015–01
HD 96700	5845.0	13.0	4.22	0.02	–4.9378	0.0035	2004–01 to 2017–07	2004–01 to 2015–04
HD 97037	5883.0	14.0	4.15	0.02	–4.9815	0.0039	2004–01 to 2017–02	2004–01 to 2015–01
HD 97343	5410.0	20.0	4.39	0.03	–5.0374	0.0033	2004–01 to 2018–05	2004–01 to 2015–05
HD 98281	5381.0	23.0	4.43	0.04	–4.9154	0.0029	2004–01 to 2016–03	2004–01 to 2015–03

This paper has been typeset from a TEX/LATEX file prepared by the author.